Netrin/UNC-6 triggers actin assembly and non-muscle myosin activity to drive dendrite retraction in the self-avoidance response.

Lakshmi Sundararajan,[1] Cody J. Smith,[1,2] Joseph D. Watson[3,4], Bryan A. Millis[1,5,6], Matthew J. Tyska,[1] David M. Miller, III[1,4,7]

[1]Department of Cell and Developmental Biology, Vanderbilt University, Nashville, TN

[2] Current address: Department of Biological Sciences, Notre Dame University, South Bend, IN

[3]Current address: Rho, Chapel Hill, NC

[4]Neuroscience Graduate Program, Vanderbilt University, Nashville, TN

[5] Cell Imaging Shared Resource, Vanderbilt University, Nashville, TN

[6] Vanderbilt Biophotonics Center, Vanderbilt University, Nashville, TN

[7]Corresponding author

SUMMARY

Dendrite growth is constrained by the self-avoidance response but the downstream pathways that balance these opposing mechanisms are unknown. We have proposed that the diffusible cue UNC-6(Netrin) is captured by UNC-40 (DCC) for a short-range interaction with UNC-5 to trigger self-avoidance in the *C. elegans* PVD neuron. Here we report that the actin-polymerizing proteins UNC-34(Ena/VASP), WSP-1(WASP), UNC-73(Trio), MIG-10(Lamellipodin) and the Arp2/3 complex effect dendrite retraction in the self-avoidance response mediated by UNC-6(Netrin). The paradoxical idea that actin polymerization results in shorter rather than longer dendrites is explained by our finding that NMY-1 (non-muscle myosin II) is necessary for retraction and could therefore mediate this effect in a contractile mechanism. Our results also show that dendrite length is determined by the antagonistic effects on the actin cytoskeleton of separate sets of effectors for retraction mediated by UNC-6(Netrin) versus outgrowth promoted by the DMA-1 receptor. Thus, our findings suggest that the dendrite length depends on an intrinsic mechanism that balances distinct modes of actin assembly for growth versus retraction.

INTRODUCTION

Dendritic arbors are defined by the balanced effects of outgrowth which expands the structure versus retraction which constrains the size of the receptive field. Microtubules and filamentous actin (F-actin) are prominent dendritic components and have been implicated as key drivers of dendritic growth and maintenance by the finding that treatments that perturb cytoskeletal dynamics may also disrupt dendritic structure [1-3]. For many neurons, dendritic growth is highly exuberant with multiple tiers of branches projecting outward from the cell soma. Ultimately, growth may be terminated by external cues. For example, neurons with similar functions are typically limited to separate domains by tiling mechanisms in which mutual contact induces dendrite retraction. The related phenomenon of self-avoidance is widely employed to prevent overlaps among sister dendrites arising from a single neuron [4]. Homotypic interactions between the membrane components Dscam and protocaderins can mediate the self-avoidance response [5-7]. Surprisingly, in some instances, soluble axon guidance cues and their canonical receptors are also required. For example, self-avoidance for the highly-branched Purkinje neuron depends on both protocadherins and also repulsive interactions between sister dendrites decorated with the Robo receptor and its diffusible ligand, Slit [8]. In another example, we have shown that UNC-6/Netrin and its cognate receptors, UNC-5 and UNC-40/DCC, mediate self-avoidance for PVD nociceptive neurons in *C. elegans* [9]. Although multiple cell-surface interactions are now known to trigger self-avoidance, little is known of the downstream effectors that drive dendrite retraction in this mechanism.

The PVD neurons, one on each side of the body, build complex dendritic arbors through a series of successive 1°, 2°, 3° and 4° orthogonal branching events [10][11,12]. Self-avoidance ensures that adjacent 3° branches do not overgrow one another[9,11] (Figure 1). Our previous results

66 suggested a novel mechanism of self-avoidance in which UNC-40/DCC captures UNC-6/Netrin
67 at the PVD cell surface and then triggers retraction by interacting with UNC-5 on the neighboring
68 3º branch. UNC-40/DCC may also effect self-avoidance by acting in a separate pathway that does
69 not involve UNC-6/Netrin[9]. Here we describe a cell biological model of dendrite retraction in
70 the PVD self-avoidance response that depends on actin polymerization.

71 The structure of the actin cytoskeleton is controlled by a wide array of effector proteins that
72 regulate specific modes of actin polymerization. For example, Ena/VASP enhances F-actin
73 elongation at the plus-end [13] and the Arp2/3 complex functions with WASP (Wiskott-Aldrich
74 syndrome protein) and the Wave Regulatory Complex (WRC) to promote F-actin branching[14].
75 Upstream regulators of WASP and the WRC include Rho family GTPases[15] and their
76 activators, the GEFs (Guanine nucleotide Exchange Factors) UNC-73/Trio[16,17] and TIAM (T-
77 cell Lymphoma Invasion and Metastasis Factor) [18,19]. Members of the Lamellipodin/Lpd
78 family recruit Ena/VASP to localize F-actin assembly at the leading edge of migrating cells[20].
79 The fact that all of these components (UNC-34/Ena/VASP, Arp2/3 complex, WSP-1/WASP,
80 WRC, UNC-73/Trio, TIAM/TIAM-1, MIG-10/lamellipodin) have been previously shown to
81 function in *C. elegans* to mediate axon guidance underscores the key role of the actin
82 cytoskeleton in growth cone steering [16,19,21-24].

83

84 Our results show that Ena/VASP functions downstream of UNC-5 to mediate PVD self-avoidance.
85 Genetic evidence detecting roles for the Arp2/3 complex and its upstream regulator, WASP/WSP-
86 1, indicates that the formation of branched actin networks may contribute to dendrite retraction.
87 A necessary role for actin polymerization is also indicated by the defective PVD self-avoidance

88 response of mutants with disabled UNC-73/Trio or MIG-10/lamellipodin. We show that PVD self-
89 avoidance also requires NMY-1/non-muscle myosin II which we propose effects dendrite
90 retraction in a contractile mechanism that drives the reorganization of the nascent actin
91 cytoskeleton. The necessary role for myosin could explain how actin polymerization can result in
92 shorter rather than longer dendrites in the self-avoidance response. Thus, we propose that UNC-
93 6/Netrin triggers self-avoidance by simultaneously stimulating actin assembly and non-muscle
94 myosin activity in 3° dendrites.
95
96 Because dendrite growth depends on actin polymerization, our finding that the actin cytoskeleton
97 is also necessary for dendrite self-avoidance points to different modes of actin polymerization for
98 growth vs retraction. Recent work has shown that a multicomponent complex involving the PVD
99 membrane proteins DMA-1 and HPO-30 drives dendritic growth by linking the PVD actin
100 cytoskeleton to adhesive cues on the adjacent epidermis[25]. Dendrite elongation, in this case,
101 depends on the WRC and TIAM-1, both of which are known to promote actin polymerization. In
102 contrast, our work has revealed that effectors of actin polymerization that are required for 3^{0} branch
103 self-avoidance (e.g., UNC-34/Ena/VASP, MIG-10/lamellipodin, UNC-73/Trio, Arp2/3 complex,
104 WSP-1/WASP) are not necessary for 3^{0} dendrite outgrowth. Additionally, we show that UNC-
105 6/Netrin signaling antagonizes the DMA-1-dependent mechanism of dendritic growth. These
106 findings are significant because they suggest that overall dendrite length is defined by the relative
107 strengths of opposing pathways that utilize separate sets of effectors to differentially regulate actin
108 polymerization for either growth or retraction.
109

110 **RESULTS**

111 **UNC-6/Netrin mediates PVD sister dendrite self-avoidance.**

112 To visualize PVD morphology, we utilized a previously characterized GFP marker driven by a
113 PVD-specific promoter (*PVD*::GFP) (Figure 1A-B)[11]. Each PVD neuron adopts a stereotypical
114 morphology characterized by a series of orthogonal junctions between adjacent branches: 1°
115 dendrites extend laterally from the PVD cell soma; each 2° dendrite projects along the dorsal-
116 ventral axis to generate a T-shaped junction comprised of two 3° dendrites each with either an
117 anterior or posterior trajectory; terminal 4° dendrites occupy interstitial locations between the
118 epidermis and body muscles. The net result of this branching pattern is a series of tree-like
119 structures or menorahs distributed along the 1° dendrite. In contrast to the highly branched
120 dendritic architecture, a single axon projects from the PVD cell soma to join the ventral nerve
121 cord[10-12]. Despite the complexity of this network, dendrites rarely overlap (~2%) in the mature
122 PVD neuron (Figure 1A). Self-avoidance depends on an active process in which sister PVD
123 dendrites retract upon physical contact with one another (Figure 1C). In the wild type, 3° branches
124 arising from adjacent menorahs initially grow outward toward one another but then retract after
125 mutual contact. The net result is a characteristic gap between the tips of 3° dendrites in neighboring
126 menorahs[11]. We have previously shown that this outcome depends in part on the diffusible cue
127 UNC-6/Netrin and its canonical receptors, UNC-40/DCC and UNC-5[9]. Mutations that disable
128 *unc-6*, for example, result in a significant increase in the fraction of overlapping 3° dendrites
129 (arrowheads, Figure 1B, Figure 2D). Similar self-avoidance defects were observed for mutants of
130 either *unc-40* or *unc-5*. Our results are consistent with a model in which UNC-40 captures UNC-
131 6 for contact with UNC-5 at the tips of adjacent 3° dendrites (Figure 1D)[9]. Here we address the

132 question of how the activated UNC-5 receptor then modifies the actin cytoskeleton to drive
133 dendrite retraction.
134
135 **Constitutively active UNC-5 drives dendrite retraction:**
136 We have proposed that UNC-6 triggers dendrite retraction by activating UNC-5[9]. This model
137 predicts that a constitutively active form of UNC-5 should result in a 'hyper'-retraction phenotype.
138 To test this idea, we attached a myristoylation sequence to the cytoplasmic domain of UNC-5[26].
139 The resultant MYR::UNC-5 protein is effectively tethered to the cytoplasmic membrane thus
140 inducing activation of the UNC-5 intracellular domain. Expression of MYR::UNC-5 in PVD
141 results in substantially shorter 3° dendrites in comparison to wild type at the late L3 stage (Figure
142 2A-C). This phenotype suggests that constitutive activation of UNC-5 prevents normal outgrowth
143 of 3° dendrites. We tested this idea by scoring the dynamic status of 3° dendrites. To quantify
144 movement, we measured the distance from a fiduciary point to the tip of a 3° dendrite at intervals
145 over time (delta t = 240 sec) (Figure 2E) (Movies S1-S2). Examples of these measurements are
146 shown in Figure 2E. We observed that wild-type 3° dendrites typically display saltatory movement
147 with periodic bouts of extension and retraction that result in net elongation. In contrast, 3° dendrites
148 of PVD neurons expressing MYR::UNC-5 grow more slowly and rarely show periods of active
149 extension and retraction (Figure 2E and 2F). The higher overall motility of 3^0 dendrites in wild-
150 type vs MYR::UNC-5 is evident from a comparison of the standard deviation of the net movement
151 of 3° dendrites from a fiduciary point in each strain (Figure 2F). Because MYR::UNC-5 lacks the
152 UNC-5 extracellular ligand-binding domain, it should function independently of *unc-6*. We
153 confirmed this prediction by demonstrating that MYR::UNC-5 rescues the self-avoidance defects
154 observed in an *unc-6* mutant background (Figure 2G). Together, these results are consistent with

155 the hypothesis that UNC-6/Netrin triggers the self-avoidance response by activating the
156 downstream UNC-5 receptor to drive dendrite retraction.
157
158 **UNC-34/Ena/VASP mediates self-avoidance in actin-containing PVD dendrites.**
159 To explore potential modifications of the PVD cytoskeleton as effectors of the UNC-6/Netrin-
160 dependent self-avoidance response, we used live cell markers to visualize actin (PVD::ACT-
161 1::GFP) and microtubules (*pdes-2*::TBA-1::mCherry) in PVD[27]. We observed a robust ACT-
162 1::GFP signal throughout the PVD neuron including the axon and all dendrites (Figure 3A). In
163 contrast, the TBA-1::mCherry signal was strongest in the PVD axon and 1° dendrite. This result
164 confirms an earlier report suggesting that dendritic microtubules are most abundant in the 1°
165 branch (Figure 3A) [27]. We thus considered the possibility that the self-avoidance response could
166 depend on the regulation of actin dynamics. To test this idea, we examined the PVD self-avoidance
167 phenotype for a mutation that disables the actin binding protein, Ena/VASP. Ena/VASP promotes
168 the elongation of actin filaments and the *C. elegans* homolog UNC-34[28] is enriched in a gene
169 expression profile of PVD neurons[11]. A strong loss-of-function allele of *unc-34*/Ena/VASP [29]
170 alters overall PVD morphology (e.g., truncated or misplaced 1^{O} dendrite, fewer 2^{O} branches)
171 (Figure 3B-C, Figure S1) but does not produce the severe lateral branching defects arising from
172 mutations in other regulators of actin polymerization (e.g, *tiam-1*) that promote dendrite
173 outgrowth[25]. Notably, PVD neurons in *unc-34* mutant animals showed robust self-avoidance
174 defects (Figure 3B-C). PVD-specific expression of mCherry-tagged UNC-34 protein rescued this
175 *unc-34* mutant phenotype suggesting that *unc-34* function is cell-autonomous for the self-
176 avoidance response (Figure 3C). *unc-34* mutant 1^{O} and 2^{O} branch defects were not rescued by PVD
177 expression of UNC-34, however, which is indicative of UNC-34 function in other nearby cell types

178 that influence PVD morphogenesis (Figure 3B, Figure S1). A downstream role for *unc-34* in the
179 UNC-6/Netrin pathway is consistent with our finding that the Unc-34 self-avoidance defect is
180 epistatic to the hyper-retraction phenotype of MYR::UNC-5 (Figure 3C).
181
182 For visualizing UNC-34/Ena/VASP in developing dendrites, we labeled UNC-34 with mCherry
183 and co-expressed it in PVD (PVD::mCherry::UNC-34) with LifeAct::GFP to detect actin-
184 containing structures. mCherry::UNC-34 is functional because it rescues the *unc-34* self-
185 avoidance defect (Fig 3C). iSIM super resolution imaging detected punctate mCherry::UNC-34
186 throughout the PVD dendritic architecture. Notably, mCherry::UNC-34 puncta are frequently
187 detected at the tips of 3° dendrites (Figure 4A-C), a finding consistent with the observed distal
188 location of Ena/VASP in F-actin containing filopodial structures [30,31]. We used time-lapse
189 imaging to detect potential trafficking of mCherry::UNC-34. Kymographs detected anterograde
190 as well as retrograde movements of mCherry::UNC-34 in 3° dendrites near the tip (green
191 arrowheads) whereas stationary puncta were characteristically located in the shaft region (red
192 arrowheads) (Figure 4C-D). These results are consistent with the idea that UNC-34/Ena/VASP is
193 delivered to 3° dendrites where it mediates actin assembly for branch retraction in the self-
194 avoidance response.
195
196 **Mutations that disable actin-polymerizing proteins disrupt dendrite self-avoidance.**
197 Genetic tests of additional regulators of actin polymerization also revealed PVD self-avoidance
198 phenotypes. Lamellipodin (Lpd) interacts with ENA/VASP at the tips of filopodia and
199 lamellopodia to extend actin filaments. Mutants of *mig-10*/Lpd display robust PVD self-avoidance
200 defects (Figure 3B, E). Similarly, self-avoidance is disrupted by a mutation that eliminates the Rac

201 GEF activity of UNC-73/Trio, a potent regulator of actin dynamics[16]. We note that both *mig-*
202 *10*/Lpd and *unc-73*/Trio mutants also show other defects in PVD morphology (e.g., displaced 1^{O}
203 dendrite, fewer 2^{O} branches) (Figure S1) but do not impair outgrowth of higher order dendrites as
204 was also observed for *unc-34* (**Fig. 3**). To test for potential roles for branched actin polymerization,
205 we examined a null allele of *wsp-1/WASP* (Wiskott-Aldrich Syndrome protein) and observed
206 defective PVD self-avoidance. If *wsp-1*/WASP functions in a common pathway with *unc-6*, then
207 the self-avoidance defect of the double mutant, *wsp-1; unc-6*, should be no more severe than that
208 of either *wsp-1* or *unc-6* single mutants. We confirmed this prediction by scoring PVD self-
209 avoidance in *wsp-1; unc-6* mutant animals (Figure 3D). Because WASP is known to activate the
210 Arp2/3 complex[15,32], we also performed RNAi knock down of the conserved Arp2/3
211 component ARX-5/p21 and detected significant PVD self-avoidance defects (Figure 3E). The
212 canonical roles of WASP and the Arp2/3 complex suggest that self-avoidance depends on the
213 formation of branched F-actin networks. Recent studies have shown that actin is required for PVD
214 dendrite outgrowth[25]. Here our genetic results point to the paradoxical idea that elongation and
215 branching of F-actin filaments are also necessary for dendrite retraction and that this mechanism
216 is activated by UNC-6/Netrin in the self-avoidance response.
217

218 **The actin cytoskeleton is highly dynamic in growing and retracting PVD dendrites.**

219 To test the idea that the actin cytoskeleton is differentially modulated for both outgrowth and
220 retraction we expressed LifeAct::GFP in PVD neurons to monitor actin dynamics during dendrite
221 morphogenesis. Although LifeAct::GFP binds both filamentous actin (F-actin) and monomeric G-
222 actin with high affinity, bright LifeAct::GFP-labeled foci typically correspond to F-actin-
223 containing structures[33]. We observed that the LifeAct::GFP signal was consistently brightest

224 nearest the tips of growing dendrites in comparison to internal dendritic regions (Fig. 5B, C) as
225 also reported in other studies [25,34]. Time-lapse imaging of PVD::LifeAct::GFP by spinning disk
226 confocal microscopy during the late L3/early L4 stage detected striking, dynamic fluctuations in
227 the LifeAct::GFP signal (Movie S3). We quantified this effect by comparing time-dependent
228 changes in LifeAct::GFP fluorescence versus that of a PVD::mCherry cytosolic marker. The
229 relatively constant intensity of PVD::mCherry signal in these experiments favors the idea that the
230 observed changes in LifeAct::GFP fluorescence could be due to actin dynamics in growing
231 dendrites (Figure 5A, D-E).
232
233 Because genetic knockdown of actin polymerizing proteins (UNC-34/Ena/VASP, MIG-10/Lpd,
234 UNC-73/Trio, WSP-1/WASP, ARX-5/P21) (**Figure 3**) disrupts self-avoidance and thus suggests
235 that F-actin is required, we monitored LifeAct::GFP in 3° dendrites during the period (L3-L4
236 transition) in which UNC-6/Netrin mediates dendrite retraction[9]. Time-lapse imaging detected
237 dynamic fluctuations in LifeAct::GFP fluorescence in these distal regions (Figure 6) (Movie S3).
238 For these measurements, the LifeAct::GFP signal near the tips of 3° dendrites was quantified at 1-
239 1.25 minute intervals over a 10 minute period spanning at least one contact event. A cytoplasmic
240 mCherry marker was used to detect contact events as instances in which the measured gap between
241 left and right 3° dendrites approached zero. In some cases, a burst of LifeAct::GFP signal was
242 detected in at least one of the adjacent dendrites during the contact period suggesting a role for
243 actin polymerization in retraction (Figure 6 A, B) (Movies S4 and S5). In other instances, however,
244 we did not observe an increase in LifeAct::GFP fluorescence with contact (Figure 6 C, D) and no
245 correlation was detected in quantitative comparisons (n = 8) between the LifeAct::GFP signal
246 before *versus* after contact (**Figure 6F**). An alternative approach for quantifying LifeAct::GFP in

247 3° dendrites at shorter time intervals (35 s) [34] also did not detect a consistent correlation between
248 LifeAct::GFP fluorescence intensity and dendrite retraction (Figure S2). The simplest explanation
249 of these results is that actin polymerization drives both outgrowth and retraction which are tightly
250 coupled over time and thus difficult to resolve as separate events.
251
252 **NMY-1/Non-muscle myosin II drives dendrite retraction in the self-avoidance mechanism.**
253 Our results indicate that F-actin is the dominant cytoskeletal structure in growing PVD dendrites
254 and that F-actin assembly is also likely required for dendrite retraction. In considering a
255 mechanism to account for dendrite shortening, we hypothesized that a newly synthesized actin
256 cytoskeleton could mediate retraction by providing a substrate for non-muscle myosin II to drive
257 contraction. To test this idea, we examined loss-of-function alleles that disable the *C. elegans* non-
258 muscle myosins, NMY-1 and NMY-2. This experiment determined that mutations in *nmy-1* but
259 not *nmy*-2 (data not shown) show PVD self-avoidance defects (Figure 7A, D). This effect is cell
260 autonomous for *nmy-1* because PVD-specific RNAi of *nmy-1* also results in overlapping 3°
261 dendrites and PVD-specific expression of GFP-tagged NMY-1 is sufficient to rescue the *nmy-1*
262 self-avoidance defect (Figure 7 B-D). We conclude that a specific non-muscle myosin, NMY-1,
263 promotes dendrite retraction in the self-avoidance mechanism and could act by driving the
264 translocation of F-actin bundles at the tips of 3° dendrites.
265
266 **Phosphomimetic activation of MLC-4 shortens PVD 3° dendrites.**
267 Non-muscle myosin II motor proteins are composed of myosin heavy chain (MHC) and light
268 chains, the essential light chain (ELC) and regulatory light chain (RLC) [35,36]. Myosin motor
269 activity is triggered by RLC phosphorylation that induces a conformational change to allow

assembly of the myosin complex into active bipolar filaments (Figure 8A) [37]. Having shown that NMY-1/non-muscle myosin is required for self-avoidance, we next performed an additional experiment to ask if constitutive non-muscle myosin activity is sufficient to induce dendrite retraction. For this test, we expressed a phosphomimetic mutant of the MLC-4, the *C. elegans* RLC homolog. MLC-4/myosin regulatory light chain contains serine/S and threonine/T phosphorylation sites in a highly-conserved domain. Both S and T residues were mutated to Aspartate/D and the resultant phosphomimetic construct MLC-4DD was fused to GFP for transgenic expression in PVD (Figure 8B-C) [38] PVD neurons that expressed MLC-4DD showed significantly shorter 3° dendrites in comparison to wild type as well as a concurrent increase in the width of gaps between 3° dendrites from adjacent menorahs (Figure 8D-G). These phenotypic traits are consistent with the proposed role of non-muscle myosin in dendrite retraction and closely resemble that of PVD neurons that express MYR::UNC-5 which functions downstream of UNC-6/Netrin to trigger the self-avoidance response. Our additional finding that MLC-4DD rescues the self-avoidance defect of *unc-6* mutants suggests that NMY-1/non-muscle myosin II also functions downstream of *unc-6* for dendrite retraction (Figure 8H).

Antagonistic pathways regulate dendrite outgrowth vs self-avoidance.

Our time lapse imaging studies detected dynamic actin polymerization in growing PVD dendrites (Movie S3). This observation and the recent finding that PVD dendritic architecture is significantly perturbed by mutations in either a specific actin structural gene, *act-4*, or that disable the F-actin nucleating WAVE complex or TIAM-1/GEF, suggest that dendritic outgrowth depends on actin assembly[25]. Actin assembly is also likely required for dendrite retraction given our results showing that genetic knockdown of a separate set of actin-binding proteins (i.e., UNC-

293 34/Ena/VASP, MIG-10/Lpd, UNC-73/Trio, WSP-1/WASP, ARX-5/p21) (**Fig. 3**), blocks self-
294 avoidance but not dendrite outgrowth [34]. A shared role for actin polymerization in both
295 outgrowth and retraction argues that the net length of PVD dendrites must depend on an intrinsic
296 mechanism that regulates actin assembly to balance these competing effects.
297
298 Our results suggest that UNC-6/Netrin signaling promotes dendrite retraction in a mechanism
299 involving F-actin assembly. PVD dendritic outgrowth is driven by a separate pathway in which
300 DMA-1, a membrane protein expressed in PVD, interacts with a multicomponent receptor
301 anchored in the adjacent epidermis[39-43]. Dendritic growth depends on binding of DMA-1 and
302 the claudin-like protein, HPO-30, to specific regulators of actin assembly (i.e., WAVE complex,
303 TIAM-1/GEF) in the PVD cytoplasm[25,44]. These interactions may be modulated by the Furin
304 KPC-1 which antagonizes DMA-1 surface expression in PVD [45-47]. *kpc-1* activity is proposed
305 to temporally weaken adhesion with the epidermis to facilitate changes in trajectory at specific
306 stages in dendritic outgrowth [41,47]. For example, the tips of 3° branches typically execute a
307 right-angle turn after the self-avoidance response to produce a 4° dendrite[11]. This morphological
308 transition largely fails in *kpc-1* mutants in which 3° dendrites elongate abnormally and show severe
309 self-avoidance defects due to over-expression of DMA-1 [41,47]. Thus, we considered the idea
310 that self-avoidance is achieved by the combined effects of *kpc-1*-dependent downregulation of
311 DMA-1 and a separate mechanism that antagonizes outgrowth and requires UNC-6/Netrin. We
312 performed a series of genetic experiments to test this model.
313
314 The hypomorphic loss-of-function allele, *kpc-1(xr58),* results in over-expression of DMA-1 and a
315 consequent, robust self-avoidance defect with ~42% of sister 3° branches overlapping one another

316 (Figure 9A, D)[46,47]. This defect is not observed, however, in *kpc-1*/+ heterozygotes (Figure
317 9D). Similarly, self-avoidance in *unc-6*/+ heterozygous animals is indistinguishable from wild
318 type (Figure 9D). Thus, a 2-fold reduction in gene dosage for either *kpc-1* or *unc-6* does not perturb
319 self-avoidance. We reasoned, however, that if expression of UNC-6/Netrin and KPC-1 were
320 simultaneously reduced by half, then self-avoidance should be at least partially disabled since both
321 *unc-6* and *kpc-1* normally function to antagonize dendrite outgrowth. To test this prediction, we
322 constructed double heterozygous mutants of *kpc-1* and *unc-6* (e.g., *kpc-1*/+*; unc-6*/+) and
323 quantified the self-avoidance phenotype. This experiment revealed that ~30% of adjacent sister 3°
324 dendrites fail to self-avoid in *kpc-1*/+*; unc-6*/+ animals which is significantly greater than that of
325 either *kpc-1*/+ or *unc-6*/+ single mutants (Figure 9B, D). This genetic "enhancer" effect is
326 consistent with the idea that both KPC-1 and UNC-6 function to limit overgrowth of 3° dendrites.
327 If this effect is due to elevated levels of DMA-1 arising from reduced KPC-1 activity in the *kpc-*
328 *1*/+*; unc-6*/+ background, then a concomitant diminution of DMA-1 activity could restore normal
329 self-avoidance. We tested this idea by constructing the triple heterozygote, *kpc-1* +/+ *dma-1; unc-*
330 *6*/+, and detected robust suppression of the self-avoidance defect observed in *kpc-1*/+*; unc-6*/+
331 animals (Figure 9C, D). Thus, these results suggest that DMA-1-mediated adhesion to the
332 epidermis antagonizes UNC-6/Netrin-driven dendrite retraction and that the relative strengths of
333 these opposing pathways must be finely tuned to achieve the self-avoidance effect (Figure 9E).
334 The key role of actin polymerization in both UNC-6/Netrin-mediated retraction and DMA-1-
335 dependent outgrowth argues that this balancing mechanism likely regulates both modes of actin
336 assembly.
337

338 **DISCUSSION**

339

340 Dendrites arising from the same neuron typically do not overlap. This phenomenon of dendrite
341 self-avoidance is universally observed and derives from an active mechanism in which contact
342 between sister dendrites triggers mutual retraction[4] As might be predicted for an event that
343 depends on physical proximity, cell-surface associated proteins have been shown to mediate
344 dendrite self-avoidance[34,48]. These include Dscam and protocadherins which are expressed in
345 multiple alternative forms to distinguish self from non-self among contacting dendrites [5-7]. Self-
346 avoidance for certain neurons can also depend on the interaction of diffusible cues with their
347 cognate receptors. For example, we have shown that the axon guidance signal, UNC-6/Netrin, and
348 its receptors, UNC-5 and UNC-40/DCC, function together to mediate self-avoidance for PVD
349 sensory neurons in *C. elegans*. We have proposed that UNC-40/DCC captures UNC-6/Netrin on
350 the membrane surface to facilitate repulsion through physical interaction with UNC-5 on PVD
351 dendrites[9] (Figure 1D). Little is known, however of the downstream effectors of dendrite
352 retraction in the self-avoidance response. Here we report that UNC-6/Netrin promotes actin-
353 polymerization to drive dendrite retraction. Our finding that non-muscle myosin is also involved
354 resolves the paradoxical observation that UNC-6/Netrin dependent actin polymerization shortens
355 rather than lengthens PVD 3° dendrites. We propose that non-muscle myosin engages the F-actin
356 cytoskeleton at the tips of PVD dendrites to drive retraction.

357

358 **Regulators of actin polymerization are required for dendrite self-avoidance.**

359 The proposed role for actin polymerization in the self-avoidance response derives from our finding
360 that multiple regulators of F-actin assembly are necessary for efficient dendrite retraction. For

361 example, a mutation that disables UNC-34, the *C. elegans* homolog of Ena/VASP, disrupts PVD
362 self-avoidance. Ena/VASP promotes actin polymerization by preventing capping proteins from
363 blocking the addition of actin monomers to the plus-end of elongating actin filaments. In axon
364 growth cones, Ena/VASP localizes to the tips of actin bundles in growing filopodia[13,31]. We
365 observed punctate Ena/VASP localization in PVD dendrites and active trafficking from the cell
366 soma (Figure 4). Our results showing that an *unc-34* mutant blocks the hyper-retraction phenotype
367 of a constitutively active UNC-5 receptor (Figure 3) argues that *unc-34* functions downstream to
368 mediate UNC-6/Netrin-dependent self-avoidance. Additional genetic evidence indicates that
369 WSP-1/WASP also acts in a common pathway with UNC-6/Netrin (Figure 3). The established role
370 for WASP of activating the Arp2/3 complex [49] is consistent with our finding that RNAi
371 knockdown of *arx-5/p21*, a conserved Arp2/3 component, partially disables the self-avoidance
372 mechanism (Figure 3). Dual roles for UNC-34 and WSP-1 in actin polymerization, as suggested
373 here, are consistent with previous work indicating that Ena/VASP can activate Arp2/3 through
374 direct interaction with WASP proteins[28,50-52]. Thus, taken together, our results suggest that
375 Ena/VASP and WSP-1 coordinate the creation of branched actin networks at the tips of retracting
376 PVD dendrites in the UNC-6/Netrin dependent self-avoidance response (Figure 9E).
377
378 A role for Ena/VASP in dendrite retraction, as have we have proposed here, parallels earlier
379 findings of a necessary function for Ena/VASP in growth cone repulsion. For example, axon
380 guidance defects arising from ectopic expression of UNC-5 in *C. elegans* touch neurons requires
381 UNC-34/Ena/VASP[53], a finding confirmed by our observation that the dendritic shortening
382 phenotype induced by MYR::UNC-5 is prevented by a loss-of-function mutation in *unc-34*.
383 Ena/VASP is also required for axon repulsion mediated by Slit and its receptor Robo[21,54,55].

384 Although Ena/VASP function can be readily integrated into models of axonal attraction, the well-
385 established role of Ena/VASP in F-actin assembly has been more difficult to rationalize in
386 mechanisms of axonal repulsion which are presumed to involve actin depolymerization[13,56]. A
387 partial explanation for this paradox is provided by a recent study showing that Slit, acting through
388 Robo, induces transient filopodial outgrowth in migrating axonal growth cones and that this effect
389 requires Ena/VASP[55]. The functional necessity for filopodial growth in this mechanism is
390 unclear, but the central role of Ena/VASP-induced actin assembly in the overall repulsive response
391 to Slit mirrors our finding that dendrite retraction in PVD neurons requires UNC-34/Ena/VASP
392 and F-actin assembly.
393
394 Our studies also detected necessary roles in self-avoidance for MIG-10/LPD which has been
395 previously shown to function with UNC-34/Ena/VASP to promote F-actin polymerization and
396 UNC-73/Trio, a Rho/Rac GEF that acts in UNC-6/Netrin pathways to regulate the actin
397 cytoskeleton[16,20,21,26]. Altogether, our genetic analysis identified five known effectors of actin
398 polymerization (UNC-34/Ena/VASP, WSP-1/WASP, Arp2/3 complex, MIG-10/Lpd, UNC-
399 73/Trio) that drive retraction of 3° dendrites in the self-avoidance response but which are not
400 required for 3° branch extension during outgrowth.
401
402 **Non-muscle myosin II drives dendrite retraction in the self-avoidance response.**
403 Our genetic analysis detected a cell-autonomous role for NMY-1/non-muscle myosin II in dendrite
404 self-avoidance (Figure 7). Because our results revealed F-actin at the tips of PVD dendrites (Figure
405 5, 6), we suggest that NMY-1 mediates retraction by interacting with F-actin to drive a contractile
406 mechanism. For example, NMY-1 could accelerate retrograde flow, a non-muscle myosin-

407 dependent effect that also drives filopodial retraction in growth cones and at the leading edge of
408 migrating cells[57,58]. Alternatively, NMY-1 could shorten PVD dendrites by inducing the
409 reorganization of the nascent actin cytoskeleton into a more compact structure[59].
410 Phosphorylation of myosin regulatory light chain (RLC) activates non-muscle myosin[37] and we
411 showed that MLC-4DD, a phosphomimetic, and, thus, constitutively active form of the *C. elegans*
412 homolog of RLC, results in hyper-retraction of PVD 3º dendrites (Figure 8). The excessive
413 retraction induced by chronic activation of MLC-4 suggests a model in which NMY-1 function is
414 selectively triggered by contact between sister dendrites and subsequent UNC-6/Netrin signaling.
415 A downstream function for non-muscle myosin II in the UNC-6/Netrin pathway is consistent with
416 our finding that the Unc-6 self-avoidance defect is rescued by MLC-4DD (Figure 8). Parallel roles
417 for these components in axon guidance are suggested by recent results showing that non-muscle
418 myosin II is required for Slit and Netrin-dependent midline avoidance in the developing vertebrate
419 spinal cord[60]. Similarly, non-muscle myosin II mediates Semaphorin-induced axonal repulsion.
420 The mechanism of Semaphorin action in this case also involves the assembly of actin bundles in
421 the axon shaft presumably to facilitate non-muscle myosin-driven retraction[61-63]. Thus, our
422 findings suggest that key drivers of axonal repulsion including nascent actin assembly and non-
423 muscle myosin may also mediate dendrite retraction in the self-avoidance response.
424
425 RLC phosphorylation activates non-muscle myosin II by releasing myosin monomers for
426 assembly into bipolar structures or myosin "stacks" that interact with actin filaments to induce
427 translocation[37,64]. Although our results are consistent with a necessary role for non-muscle
428 myosin in dendrite retraction, the tips of PVD 3º dendrites are likely too narrow (~50 nm) [65] to
429 accommodate myosin stacks (~300 nm) [64,66]. We suggest that the actin-branching function of

430 Arp2/3, which we have shown mediates PVD dendrite retraction, could induce transient
431 expansion of the dendritic tip to allow assembly of myosin stacks. In this model, actin-
432 polymerization involving Arp2/3 could effectively limit ectopic NMY-1 activation in the
433 dendritic shaft by restricting the assembly of myosin stacks to the tips of contacting sister
434 dendrites. Alternatively, recent evidence indicates that myosin can also induce contraction in its
435 monomeric or unpolymerized form[67] which should have ready access to the dendrite tip. This
436 idea is consistent would our observation that GFP-tagged NMY-1 is active (e.g., rescues the self-
437 avoidance defect of *nmy-1*) and did not display the punctate appearance characteristic of myosin
438 stacks (Fenix et al., 2016) but is diffusely localized throughout the PVD cytoplasm (Figure 7B).
439

440 **Parallel-acting pathways drive dendrite self-avoidance.**

441 Although self-avoidance is perturbed in UNC-6/Netrin pathway mutants, a significant fraction
442 (~70%) (Figure 2D) of PVD 3º dendrites show apparently normal self-avoidance behavior[9]. One
443 explanation for this observation is provided by the recent discovery of an independent pathway,
444 mediated by MIG/14/Wntless, that is necessary for self-avoidance in an additional fraction of PVD
445 3º dendrites[34]. Parallel acting pathways also mediate self-avoidance in mammalian Purkinje
446 neurons where slit-robo signaling acts in concert with protocadherins (Gibson et al., 2014;
447 Lefebvre et al., 2012). The likelihood of additional effectors of self-avoidance is also suggested
448 by the incompletely penetrant effects of Dscam mutants in Drosophila sensory neuron self-
449 avoidance (Matthews and Grueber, 2011). Thus, our results in *C. elegans* mirror findings in other
450 organisms which together suggest that multiple mechanisms have evolved to insure dendrite self-
451 avoidance.
452

453 **The actin cytoskeleton is highly dynamic in growing and retracting PVD dendrites.**

454 We used time-lapse imaging with LifeAct::GFP, a live-cell marker for actin {Riedl:2008gw}, to
455 monitor actin PVD dendrites. The LifeAct::GFP signal is typically brighter near the distal ends of
456 growing branches in comparison to interstitial regions (Figure 5) and is highly dynamic (Movie
457 S3). The distal localization and rapidly fluctuating LifeAct::GFP signal in PVD dendrites
458 resembles recently reported "actin blobs" that actively migrate in Drosophila sensory neurons with
459 complex dendrite arbors and that appear to presage points of branch initiation [68].

460

461 **Antagonistic pathways regulate dendrite outgrowth vs retraction.**

462 Dendritic architecture is defined by the combined effects of outgrowth which expands the arbor vs
463 retraction which limits the size of the receptive field. This interaction of positive and negative
464 effects is readily observed in the development of 3º PVD dendrites. Initially, 3º dendrites
465 emanating from adjacent menorahs grow out along the body axis until contacting one another and
466 then retract to avoid overlap[9,11]. Outgrowth in this case is promoted by a multicomponent
467 receptor-ligand complex that mediates adhesive interactions with the adjacent epidermis (Díaz-
468 Balzac et al., 2016; Dong et al., 2013; Salzberg et al., 2013; Zou et al., 2016) (Figure 9E). When
469 this pathway is dysregulated by over-expression of the DMA-1 receptor in PVD neurons, for
470 example, 3º dendrites continue to adhere to the epidermis and overgrow one another[47,69]. 3º
471 branch self-avoidance also fails in mutants that disable UNC-6/Netrin signaling which we have
472 shown promotes dendrite retraction[9]. Thus, these results suggest that the net length and
473 placement of each 3º branch depends on the balanced effects of locally acting signals that either
474 extend (e.g., DMA-1) or shorten (e.g., UNC-6/Netrin) the dendrite. We confirmed this idea in
475 genetic experiments that detected strong dose-sensitive interactions between these opposing

476 pathways. For example, a 50% reduction of UNC-6/Netrin expression in a heterozygous *unc-6/+*
477 mutant does not perturb self-avoidance. Similarly, a genetic mutant (*kpc-1/+)* that partially
478 elevates DMA-1 also shows normal 3º branch outgrowth. The combination of both mutations in
479 the double heterozygote, *unc-6/+; kpc-1/+,* however, produces a strong self-avoidance defect. Our
480 genetic results identified multiple regulators of actin polymerization (UNC-34/Ena/VASP, WSP-
481 1/WASP, ARX-5/p21, MIG-10/Lamelipodin, UNC-73/Trio) that are required for self-avoidance.
482 We thus propose that UNC-6/Netrin promotes actin polymerization to drive dendrite retraction
483 and that non-muscle myosin II interacts with a nascent actin cytoskeleton to translocate each 3º
484 dendrite away from its neighbor. F-actin is also abundant and highly dynamic in growing PVD
485 dendrites. Notably, a different set of F-actin promoting factors (WRC, TIAM/GEF) interacts with
486 the DMA-1 receptor complex to drive PVD dendritic growth (Figure 9E) [25]. Thus, the challenge
487 for future studies is to elucidate the cell biological machinery through which opposing pathways
488 manipulate the actin cytoskeleton to effect either dendrite growth or retraction.
489
490

491 **MATERIALS AND METHODS**

492

493 **Strains and genetics**

494 All the strains used were maintained at 20°C and cultured as previously described (Brenner, 1974).

495 We used the N2 Bristol strain as wild-type.

496

497 The previously described strains used in this study include: NC1404 [*wdIs52* (*pF49H12.4*::GFP)]

498 ,NW434 [*unc-6(ev400)X*;*wdIs52(pF49H12.4::GFP)*], TV17,200 [*kpc-1(xr58);*

499 *wyIs592(pser2prom3::GFP)*], TV9656 [*dma-1(wy686); unc-119(ed3)III;*

500 *wyEx3355(pser2prom3::GFP+odr-1::RFP)*], CX1248 [*KyEx3482* (*pdes-2::TBA-*

501 *1::mCherry+coel::RFP*)] [9], CLP928 [*twnEx382(Pser2.3::LifeAct::EGFP, Pser2.3::mCherry,*

502 *Pgcy-8::gfp)*].

503

504 Additional strains generated for this study: NC2580 *unc-34(gm104)V*; *wdIs52*, NG324 [*wsp-*

505 *1(gm324)*; *wdIs52*], *+/szT1 lon-2(e678) I;* HR1184 [*nmy-1(sb115) dpy-8(e130)/szT1 X*], NC2726

506 [*nmy-1(sb113)*;*wdIs52*], *unc-73(rh40)*]; *wdIs52*.

507 NC3284 [*wdEx1011* (*pF49H12.4*::myrUNC-5::GFP)], was produced by microinjection of

508 plasmids pLSR18 (pF49H12.4::myrUNC-5::GFP), *pmyo-2*::mCherry and pCJS04

509 (pF49H12.4::mCherry).

510 NC3048 [*wdIs98* (pF49H12.4::ACT-1::GFP)] was produced by microinjection of plasmids

511 pLSR03 (pF49H12.4::ACT-1::GFP) and *pceh-22*::GFP and integrated as previously described

512 (Miller and Niemeyer, 1995).

513 NC3085 [*wdEx967* (pF49H12.4::mCherry::UNC-34)] was obtained by microinjection of plasmids
514 pCJS78(pF49H12.4::mCherry::UNC-34) and *pmyo-2*::mCherry.
515 NC3090 [*wdEx972* (pF49H12.4::LifeAct::GFP)] was acquired by microinjecting plasmids
516 pLSR06 (pF49H12.4::LifeAct::GFP) and *pmyo-2*::mCherry.
517 NC3029 [(pF49H12.4::*nmy-1(+)* + pF49H12.4::*nmy-1(-)*)] was obtained by microinjection of
518 pLSR09 (pF49H12.4::*nmy-1(+)*), pLSR10 (pF49H12.4::*nmy-1(-)*), pmyo-2::mCherry and pCJS04
519 (pF49H12.4::mCherry)
520 NC3087 [*wdEx969* (pF49H12.4::GFP::Linker::NMY-1)] was produced by microinjecting
521 plasmids pLSR11 (pF49H12.4::GFP::Linker::NMY-1), pCJS04 (pF49H12.4::mCherry) and
522 pmyo-2::mCherry.
523 *wdEx1009* (pF49H12.4::GFP::Linker::MLC-4DD) [NC3283] was obtained by microinjection of
524 plasmids pLSR17 (pF49H12.4::GFP::Linker::MLC-4), pCJS04 (pF49H12.4::mCherry) and
525 pmyo-2::mCherry.
526
527 **Molecular Biology**:
528 **Building pLSR11 (*pF49H12.4::*GFP::Linker::NMY-1::*unc-10* 3'UTR):** We used the
529 Clonetech in-fusion HD cloning kit (Cat # 638910) to build this plasmid. The *nmy-1* genomic
530 region was amplified from pACP01 (*pF49H12.4::*NMY-1::mCherry) with overlapping regions
531 corresponding to pCJS95 (*pF49H12.4::*GFP::CED-10::*unc-10* 3'UTR). We also PCR amplified
532 pCJS95 with primers overlapping the *nmy-1* genomic sequences to swap CED-10 with NMY-1.
533 We then used the NEB site-directed mutagenesis kit to insert a 24-nucleotide glycine rich linker
534 (see Table 1). The resultant pLSR11 plasmid was sequenced to confirm that the linker was inserted
535 between the GFP sequence and *nmy-1*. See table 1 for primer sequences.

536

537 **Constructing pLSR17 (*pF49H12.4*::GFP::Linker::MLC-4DD):** We used the Clonetech in-
538 fusion HD cloning kit (Cat # 638910) to construct this plasmid. The *mlc-4* genomic region was
539 amplified from N2 DNA using primers with overlapping adapter complementary to pLSR11
540 (*pF49H12.4*::GFP::Linker::NMY-1). pLSR11 was amplified with primers containing adapter
541 sequences complementary to *mlc-4*. The amplified fragments were combined for the infusion
542 cloning to replace *nmy-1* with *mlc-4*. We then used the NEB site directed mutagenesis kit to
543 change MLC-4 codons for Serine 18 and Threonine 17 to nucleotide sequences that encode
544 Aspartate acid. The resultant pLSR17 plasmid was confirmed by sequencing.

545

546 **Confocal microscopy and image analysis**: Animals were immobilized with 15 mM levamisole/
547 0.05% tricaine and mounted on 2% agarose pads in M9 buffer as previously described [11]. Z
548 stack images were collected using a Nikon TiE inverted fluorescent microscope equipped with an
549 A1R point scanning confocal and a Plan Apo 40X 1.3NA oil immersion objective or on a Leica
550 TCS SP5 confocal microscope with a 40X or 63X objective. Z stacks were collected at either 0.5
551 or 1μm depth from the ventral nerve cord to the top of PVD cell body. Maximum projection images
552 were collated with either LAS-AF (Leica) or with NIS elements software (Nikon). Dendrite length
553 was measured using the line tool in Fiji/image J. Co-localization images were assembled using
554 image J. Z stack images that were collected using the LAS-AF or NIS elements software was
555 imported into ImageJ/Fiji for further analysis.

556

557 **TIRF microscopy and analysis.** Animals were immobilized with 15mM levamisole/ 0.05%
558 tricane and mounted on 2% agarose pads in M9 buffer. The coverslip placed on top of the agarose

559 pad encasing the immobilized worms is 1mm in thickness. Time-lapse datasets were acquired
560 using a Nikon TiE inverted fluorescence microscope outfitted with a TIRF illuminator, Apo TIRF
561 100x, 1.49NA oil immersion objective, and NIS-Elements software (Nikon Instruments, Inc.). The
562 images for the time lapse video were captured in a single plane and the TIRF angle was adjusted
563 for oblique illumination of 3° PVD dendrites . Datasets were imported into FIJI/ImageJ for further
564 analysis, including intensity quantification. The rectangle tool was used to encompass left and right
565 pairs of adjacent 3° dendrites with separate ROI (Regions of Interest) for image frame and the
566 intensities measured using the analyze tool. Resultant fluorescent intensity values were generated
567 with prism graphical software.
568
569 **iSIM super-resolution imaging and analysis**. Animals were immobilized with 0.4mM
570 levamisole and mounted on 10% agarose pads in M9 buffer. Z stack images were captured using
571 a Hamamatsu sCMOS camera on a Leica iSIM and a 100x, 1.45 NA objective. Images were
572 deconvolved and processed using Metamorph and Fiji/ImageJ.
573
574 **Spinning disk confocal microscopy:** Animals were immobilized with 0.4mM levamisole and
575 mounted on 10% agarose pads in M9 buffer. Volumes over time were captured using an automated
576 TiE inverted fluorescence microscope platform with an X1 spinning disk head (Yokogawa) and
577 DU-897 EM-CCD (Andor Technology), piezo-electric Z stage (Mad City Labs) and Apo TIRF
578 100x 1.49 NA oil immersion objective (Nikon Instruments, Inc.). Analysis of fluorescence
579 intensity was accomplished using NIS-Elements and Fiji/Image J software.
580

581 **Quantification of fluorescence intensity in growing vs. non-growing dendrites:** L2-L3 larvae
582 were immobilized with 0.4mM levamisole and mounted on 10% agarose pads in M9 buffer for
583 imaging with the spinning disk confocal microscope. Z-stacks of PVD dendrites were imaged at
584 either 1 min or 1.30 minute intervals with the 100X 1.49 NA oil immersion objective. PVD
585 dendrites (2º, 3º and 4º) undergoing outgrowth with a succession of rapid extensions and
586 retractions during the length of the time lapse videos were analyzed. NIS elements was used for
587 measurements of LifeAct::GFP from a 1μm ROI at the tips of growing dendrites. In the same
588 videos, fluorescence intensity was measured for an identical 1μm ROI of PVD branches (1º, 2º
589 and 3º) that were not undergoing outgrowth. Fluorescence intensity measurements for the
590 outgrowth and no-outgrowth datasets were normalized against the maximum overall LifeAct::GFP
591 value (Figure 5).
592
593 **Quantification of fluorescence intensity in 3º dendrites undergoing self-avoidance**: Late L3
594 larvae were immobilized as above for imaging in the spinning disk confocal microscope. Z-stacks
595 of PVD dendrites were imaged at either 1 or 1.30 minute intervals with the a 100X objective.
596 Contact is defined by the point at which the maximum ferret (i.e., gap) between adjacent PVD 3º
597 dendrites in the mCherry channel approached zero. Nikon NIS Elements was used to obtain
598 LifeAct::GFP and mCherry fluorescence measurements from a 1μm ROI at the tips of the left and
599 right 3º dendrites undergoing contact. Fluorescence intensity measurements of LifeAct::GFP and
600 mCherry for the opposing dendrites were normalized against the maximum value for each
601 fluorophore and plotted vs time (Figure 6A-E).
602 For comparisons of LifeAct::GFP signals at the tips of 3º dendrites before and during contact,
603 fluorescence intensities were determined from a 5 μm ROI centered at the point of contact and

604 from a contiguous control (non-contact) 5 μm ROI positioned either to the left or right of the
605 contact region (Figure 6F). The change in fluorescence intensity (ΔF) for each contact and control
606 region was calculated as the difference between the signal at contact (F_t) and the fluorescence
607 value at two time points prior to contact (F_{t-2}) normalized to F_{t-2} or $\Delta F = (F_t - F_{t-2})/F_{t-2}$ [34]. For
608 all measurements, the cytoplasmic mCherry marker was monitored to measure the Max Feret (in
609 this case, maximum distance between two points) between the tips of adjacent 3° dendrites and the
610 point of contact determined when the Max Feret approaches zero. Statistical comparisons (N = 8)
611 were performed with a 2-way ANOVA with Bonferroni correction.
612
613 **Statistics:** Student's t test was used for comparisons between 2 groups and ANOVA for
614 comparisons between three or more groups with either Tukey posthoc or Bonferroni correction for
615 multiple comparisons. Kolmogorov-Smirnov test was performed for comparisons between
616 frequency distributions of 3° dendrite length and gaps between 3° dendrites (Figures 2C and 8F,
617 G) .
618
619 Table 1.
620

Primer name	Primer sequences
myrunc-5 Vec. For.	CGGCCGCGGATAACAAATTTCA
myrunc-5 Vec. Rev.	GGATCCCATCCCGGGGAT
myrunc-5 Frag. For.	CCCGGGATGGGATCCATGggatcttctaagtctgctagcAAAC
myrunc-5 Frag. Rev.	TGTTATCCGCGGCCGCTATTTGTATAGTTCATCCATGCCATGTG
nmy-1 linker F1	GGATGCCCCTCCgtacagctcgtccatg

nmy-1 linker R1	GCAGGGGGAGGTGATGGGTGACCTGCAGTAC
mlc-4DD F1	CATGTTCGATCAGGCTCAAATTCAAG
mlc-4DD R1	GCGAACACATTGTCATCGGCTCTTTG
mlc-4 Vec. For.	GGATAACAAATTTCTATGTTTTTGTTTGTTTTTTGTCTTAATTACCA
mlc-4 Vec. Rev.	ACCTCCCCCTGCGGATG
mlc-4 Frag. For.	TCCGCAGGGGGAGGTATGGCCTCCCGCAAAACC
mlc-4 Frag. Rev.	agaaatttgttatccTTAAGCCTCATCCTTGTCCTTGGTTCC

ACKNOWLEDGMENTS

We thank C. Bargmann, K. Shen, J. Plastino, Dr. T.J. Kubiseski, E. Lundquist, P. Mains and H. Buelow for strains and reagents. We thank Chun-Liang Pan and Chien-Po Liao for sharing their work, reagents and advice prior to publication, Dylan Burnette and members of his laboratory, Aidan Fenix and Nilay Taneja, for helpful suggestions and members of the Miller lab for comments on the manuscript. Spinning disk images were obtained in the Nikon Center of Excellence at Vanderbilt University. This work was supported by NIH Grants R01 NS079611 to D. M. M, F31 NS071801 to C.J.S and F31 NS49743 to J. D. W. Some of the strains used in this work were provided by the *C. elegans* Genetics Center, which is supported by the US National Institutes of Health (NIH) National Center for Research Resources. L.S., C.J.S and J.D.W. performed experiments with advice from D.M.M., M.J.T. provided imaging expertise and advice; B.A.M

helped with spinning disk imaging and edited videos, L.S. and D.M.M. wrote the paper with input from coauthors.

641 **REFERENCES**

642 1. Delandre C, Amikura R, Moore AW. Microtubule nucleation and organization in
643 dendrites. cc. 2016;15: 1685–1692. doi:10.1080/15384101.2016.1172158

644 2. Jan YN, Jan LY. Branching out: mechanisms of dendritic arborization. Nat Rev
645 Neurosci. 2010;11: 316–328. doi:10.1038/nrn2836

646 3. Konietzny A, Bär J, Mikhaylova M. Dendritic Actin Cytoskeleton: Structure,
647 Functions, and Regulations. Front Cell Neurosci. 2017;11: 147.
648 doi:10.3389/fncel.2017.00147

649 4. Grueber WB, Sagasti A. Self-avoidance and tiling: Mechanisms of dendrite and
650 axon spacing. Cold Spring Harb Perspect Biol. 2010;2: a001750–a001750.
651 doi:10.1101/cshperspect.a001750

652 5. Fuerst PG, Bruce F, Tian M, Wei W, Elstrott J, Feller MB, et al. DSCAM and
653 DSCAML1 function in self-avoidance in multiple cell types in the developing
654 mouse retina. Neuron. 2009;64: 484–497. doi:10.1016/j.neuron.2009.09.027

655 6. Lefebvre JL, Kostadinov D, Chen WV, Maniatis T, Sanes JR. Protocadherins
656 mediate dendritic self-avoidance in the mammalian nervous system. Nature. Nature
657 Publishing Group; 2012;488: 517–521. doi:10.1038/nature11305

658 7. Matthews BJ, Kim ME, Flanagan JJ, Hattori D, Clemens JC, Zipursky SL, et al.
659 Dendrite self-avoidance is controlled by Dscam. Cell. 2007;129: 593–604.
660 doi:10.1016/j.cell.2007.04.013

661 8. Gibson DA, Tymanskyj S, Yuan RC, Leung HC, Lefebvre JL, Sanes JR, et al.
662 Dendrite Self-Avoidance Requires Cell-Autonomous Slit/Robo Signaling in
663 Cerebellar Purkinje Cells. Neuron. Elsevier Inc; 2014;81: 1040–1056.
664 doi:10.1016/j.neuron.2014.01.009

665 9. Smith CJ, Watson JD, Vanhoven MK, Colón-Ramos DA, Miller DM III. Netrin
666 (UNC-6) mediates dendritic self-avoidance. Nat Neurosci. 2012;15: 731–737.
667 doi:10.1038/nn.3065

668 10. Albeg A, Smith CJ, Chatzigeorgiou M, Feitelson DG, Hall DH, Schafer WR, et al.
669 C. elegans multi-dendritic sensory neurons: morphology and function. Mol Cell
670 Neurosci. 2011;46: 308–317. doi:10.1016/j.mcn.2010.10.001

671 11. Smith CJ, Watson JD, Spencer WC, O'Brien T, Cha B, Albeg A, et al. Time-lapse
672 imaging and cell-specific expression profiling reveal dynamic branching and
673 molecular determinants of a multi-dendritic nociceptor in C. elegans. Developmental
674 Biology. 2010;345: 18–33. doi:10.1016/j.ydbio.2010.05.502

675 12. Oren-Suissa M, Hall DH, Treinin M, Shemer G, Podbilewicz B. The fusogen EFF-1
676 controls sculpting of mechanosensory dendrites. Science. 2010;328: 1285–1288.
677 doi:10.1126/science.1189095

678 13. Drees F, Gertler FB. Ena/VASP: proteins at the tip of the nervous system. Current
679 Opinion in Neurobiology. 2008;18: 53–59. doi:10.1016/j.conb.2008.05.007

680 14. Goley ED, Welch MD. The ARP2/3 complex: an actin nucleator comes of age. Nat
681 Rev Mol Cell Biol. 2006;7: 713–726. doi:10.1038/nrm2026

682 15. Takenawa T, Suetsugu S. The WASP-WAVE protein network: connecting the
683 membrane to the cytoskeleton. Nat Rev Mol Cell Biol. 2007;8: 37–48.
684 doi:10.1038/nrm2069

685 16. Steven R, Kubiseski TJ, Zheng H, Kulkarni S, Mancillas J, Ruiz Morales A, et al.
686 UNC-73 activates the Rac GTPase and is required for cell and growth cone
687 migrations in C. elegans. Cell. 1998;92: 785–795.

688 17. Hu S, Pawson T, Steven RM. UNC-73/Trio RhoGEF-2 Activity Modulates
689 Caenorhabditis elegans Motility Through Changes in Neurotransmitter Signaling
690 Upstream of the GSA-1/G s Pathway. Genetics. 2011;189: 137–151.
691 doi:10.1534/genetics.111.131227

692 18. Matsuo N, Hoshino M, Yoshizawa M, Nabeshima Y-I. Characterization of STEF, a
693 guanine nucleotide exchange factor for Rac1, required for neurite growth. J Biol
694 Chem. 2002;277: 2860–2868. doi:10.1074/jbc.M106186200

695 19. Demarco RS, Struckhoff EC, Lundquist EA. The Rac GTP exchange factor TIAM-1
696 acts with CDC-42 and the guidance receptor UNC-40/DCC in neuronal protrusion
697 and axon guidance. PLoS Genetics. Public Library of Science; 2012;8: e1002665.
698 doi:10.1371/journal.pgen.1002665

699 20. Krause M, Leslie JD, Stewart M, Lafuente EM, Valderrama F, Jagannathan R, et al.
700 Lamellipodin, an Ena/VASP ligand, is implicated in the regulation of lamellipodial
701 dynamics. Developmental Cell. 2004;7: 571–583. doi:10.1016/j.devcel.2004.07.024

702 21. Chang C, Adler CE, Krause M, Clark SG, Gertler FB, Tessier-Lavigne M, et al.
703 MIG-10/lamellipodin and AGE-1/PI3K promote axon guidance and outgrowth in
704 response to slit and netrin. Curr Biol. 2006;16: 854–862.
705 doi:10.1016/j.cub.2006.03.083

706 22. Demarco RS, Lundquist EA. RACK-1 Acts with Rac GTPase Signaling and UNC-
707 115/ abLIM in Caenorhabditiselegans Axon Pathfinding and Cell Migration. PLoS
708 Genetics. 2010;6: 1–17. doi:doi:10.1371/journal.pgen.100121

709 23. Shakir MA, Jiang K, Struckhoff EC, Demarco RS, Patel FB, Soto MC, et al. The
710 Arp2/3 activators WAVE and WASP have distinct genetic interactions with Rac
711 GTPases in Caenorhabditis elegans axon guidance. Genetics. 2008;179: 1957–1971.
712 doi:10.1534/genetics.108.088963

24. Levy-Strumpf N, Culotti JG. VAB-8, UNC-73 and MIG-2 regulate axon polarity and cell migration functions of UNC-40 in C. elegans. Nature Publishing Group. 2007;10: 161–168. doi:10.1038/nn1835

25. Zou W, Dong X, Broederdorf TR, Shen A, Kramer DA, Shi R, et al. A Dendritic Guidance Receptor Complex Brings Together Distinct Actin Regulators to Drive Efficient F-Actin Assembly and Branching. Developmental Cell. 2018;45: 362–375.e3. doi:10.1016/j.devcel.2018.04.008

26. Norris AD, Sundararajan L, Morgan DE, Roberts ZJ, Lundquist EA. The UNC-6/Netrin receptors UNC-40/DCC and UNC-5 inhibit growth cone filopodial protrusion via UNC-73/Trio, Rac-like GTPases and UNC-33/CRMP. Development. 2014;141: 4395–4405. doi:10.1242/dev.110437

27. Maniar TA, Kaplan M, Wang GJ, Shen K, Wei L, Shaw JE, et al. UNC-33 (CRMP) and ankyrin organize microtubules and localize kinesin to polarize axon-dendrite sorting. Nat Neurosci. Nature Publishing Group; 2011;15: 48–56. doi:10.1038/nn.2970

28. Withee J, Galligan B, Hawkins N, Garriga G. Caenorhabditis elegans WASP and Ena/VASP proteins play compensatory roles in morphogenesis and neuronal cell migration. Genetics. 2004;167: 1165–1176. doi:10.1534/genetics.103.025676

29. Fleming T, Chien S-C, Vanderzalm PJ, Dell M, Gavin MK, Forrester WC, et al. The role of C. elegans Ena/VASP homolog UNC-34 in neuronal polarity and motility. Developmental Biology. 2010;344: 94–106. doi:10.1016/j.ydbio.2010.04.025

30. Applewhite DA, Barzik M, Kojima S-I, Svitkina TM, Gertler FB, Borisy GG. Ena/VASP proteins have an anti-capping independent function in filopodia formation. Molecular Biology of the Cell. 2007;18: 2579–2591. doi:10.1091/mbc.E06-11-0990

31. Gates J, Mahaffey JP, Rogers SL, Emerson M, Rogers EM, Sottile SL, et al. Enabled plays key roles in embryonic epithelial morphogenesis in Drosophila. Development. 2007;134: 2027–2039. doi:10.1242/dev.02849

32. Zhang W, Wu Y, Du L, Tang DD, Gunst SJ. Activation of the Arp2/3 complex by N-WASp is required for actin polymerization and contraction in smooth muscle. Am J Physiol, Cell Physiol. 2005;288: C1145–60. doi:10.1152/ajpcell.00387.2004

33. Riedl J, Crevenna AH, Kessenbrock K, Yu JH, Neukirchen D, Bista M, et al. Lifeact: a versatile marker to visualize F-actin. Nat Meth. 2008;5: 605–607. doi:10.1038/nmeth.1220

34. Liao C-P, Li H, Lee H-H, Chien C-T, Pan C-L. Cell-Autonomous Regulation of Dendrite Self-Avoidance by the Wnt Secretory Factor MIG-14/Wntless. Neuron. 2018;98: 320–334.e6. doi:10.1016/j.neuron.2018.03.031

750 35. Piekny AJ, Mains PE. Rho-binding kinase (LET-502) and myosin phosphatase
751 (MEL-11) regulate cytokinesis in the early Caenorhabditis elegans embryo. J Cell
752 Sci. 2002;115: 2271–2282.

753 36. Vicente-Manzanares M, Ma X, Adelstein RS, Horwitz AR. Non-muscle myosin II
754 takes centre stage in cell adhesion and migration. Nat Rev Mol Cell Biol. 2009;10:
755 778–790. doi:10.1038/nrm2786

756 37. Somlyo AP, Somlyo AV. Signal transduction and regulation in smooth muscle.
757 Nature. 1994;372: 231–236. doi:10.1038/372231a0

758 38. Ono K, Ono S. Two distinct myosin II populations coordinate ovulatory contraction
759 of the myoepithelial sheath in the Caenorhabditis elegans somatic gonad. Molecular
760 Biology of the Cell. American Society for Cell Biology; 2016;27: 1131–1142.
761 doi:10.1091/mbc.E15-09-0648

762 39. Zou W, Shen A, Dong X, Tugizova M, Xiang YK, Shen K. A multi-protein
763 receptor-ligand complex underlies combinatorial dendrite guidance choices in C.
764 elegans. eLife. eLife Sciences Publications Limited; 2016;5: e18345.
765 doi:10.7554/eLife.18345

766 40. Díaz-Balzac CA, Rahman M, Lazaro-Pena MI, Martin Hernandez LA, Salzberg Y,
767 Aguirre-Chen C, et al. Muscle- and Skin-Derived Cues Jointly Orchestrate
768 Patterning of Somatosensory Dendrites. Curr Biol. 2016;26: 2379–2387.
769 doi:10.1016/j.cub.2016.07.008

770 41. Liu OW, Shen K. The transmembrane LRR protein DMA-1 promotes dendrite
771 branching and growth in C. elegans. Nat Neurosci. 2011. doi:10.1038/nn.2978

772 42. Salzberg Y, Díaz-Balzac CA, Ramirez-Suarez NJ, Attreed M, Tecle E, Desbois M,
773 et al. Skin-Derived Cues Control Arborization of Sensory Dendritesin
774 Caenorhabditis elegans. Cell. Elsevier Inc; 2013;155: 308–320.
775 doi:10.1016/j.cell.2013.08.058

776 43. Dong X, Liu OW, Howell AS, Shen K. An Extracellular Adhesion Molecule
777 Complex Patterns Dendritic Branching and Morphogenesis. Cell. 2013;155: 296–
778 307. doi:10.1016/j.cell.2013.08.059

779 44. Smith CJ, O'Brien T, Chatzigeorgiou M, Spencer WC, Feingold-Link E, Husson SJ,
780 et al. Sensory Neuron Fates Are Distinguishedby a Transcriptional Switchthat
781 Regulates Dendrite Branch Stabilization. Neuron. Elsevier Inc; 2013;79: 266–280.
782 doi:10.1016/j.neuron.2013.05.009

783 45. Schroeder NE, Androwski RJ, Rashid A, Lee H, Lee J, Barr MM. Dauer-Specific
784 Dendrite Arborization in C. elegans Is Regulated by KPC-1/Furin. Current Biology.
785 Elsevier Ltd; 2013;23: 1527–1535. doi:10.1016/j.cub.2013.06.058

786 46. Salzberg Y, Ramirez-Suarez NJ, Bülow HE. The Proprotein Convertase KPC-
787 1/Furin Controls Branching and Self-avoidance of Sensory Dendrites in
788 Caenorhabditis elegans. Chisholm AD, editor. PLoS Genetics. 2014;10: e1004657–
789 13. doi:10.1371/journal.pgen.1004657

790 47. Dong X, Chiu H, Park YJ, Zou W, Zou Y, Özkan E, et al. Precise regulation of the
791 guidance receptor DMA-1 by KPC-1/Furin instructs dendritic branching decisions.
792 eLife. eLife Sciences Publications Limited; 2016;5: 308. doi:10.7554/eLife.11008

793 48. Sun LO, Jiang Z, Rivlin-Etzion M, Hand R, Brady CM, Matsuoka RL, et al. On and
794 off retinal circuit assembly by divergent molecular mechanisms. Science. 2013;342:
795 1241974–1241974. doi:10.1126/science.1241974

796 49. Pollitt AY, Insall RH. WASP and SCAR/WAVE proteins: the drivers of actin
797 assembly. J Cell Sci. The Company of Biologists Ltd; 2009;122: 2575–2578.
798 doi:10.1242/jcs.023879

799 50. Castellano F, Le Clainche C, Patin D, Carlier MF, Chavrier P. A WASp-VASP
800 complex regulates actin polymerization at the plasma membrane. EMBO J. 2001;20:
801 5603–5614. doi:10.1093/emboj/20.20.5603

802 51. Chen XJ, Squarr AJ, Stephan R, Chen B, Higgins TE, Barry DJ, et al. Ena/VASP
803 proteins cooperate with the WAVE complex to regulate the actin cytoskeleton.
804 Developmental Cell. 2014;30: 569–584. doi:10.1016/j.devcel.2014.08.001

805 52. Havrylenko S, Noguera P, Abou-Ghali M, Manzi J, Faqir F, Lamora A, et al.
806 WAVE binds Ena/VASP for enhanced Arp2/3 complex-based actin assembly.
807 Molecular Biology of the Cell. American Society for Cell Biology; 2015;26: 55–65.
808 doi:10.1091/mbc.E14-07-1200

809 53. Colavita A, Culotti JG. Suppressors of ectopic UNC-5 growth cone steering identify
810 eight genes involved in axon guidance in Caenorhabditis elegans. Developmental
811 Biology. 1998;194: 72–85. doi:10.1006/dbio.1997.8790

812 54. Bashaw GJ, Kidd T, Murray D, Pawson T, Goodman CS. Repulsive axon guidance:
813 Abelson and Enabled play opposing roles downstream of the roundabout receptor.
814 Cell. 2000;101: 703–715.

815 55. McConnell RE, Edward van Veen J, Vidaki M, Kwiatkowski AV, Meyer AS,
816 Gertler FB. A requirement for filopodia extension toward Slit during Robo-mediated
817 axon repulsion. The Journal of Cell Biology. 2016;213: 261–274.
818 doi:10.1083/jcb.201509062

819 56. Hung R-J, Terman JR. Extracellular inhibitors, repellents, and
820 semaphorin/plexin/MICAL-mediated actin filament disassembly. Cytoskeleton
821 (Hoboken). John Wiley & Sons, Inc; 2011;68: 415–433. doi:10.1002/cm.20527

822 57. Lin C, Espreafico E, Mooseker M, Forscher P. Myosin drives retrograde F-actin
823 flow in neuronal growth cones. Neuron. 1996;16: 769–782.

824 58. Mitchison TJ, Cramer LP. Actin-based cell motility and cell locomotion. Cell.
825 1996;84: 371–379.

826 59. Medeiros NA, Burnette DT, Forscher P. Myosin II functions in actin-bundle
827 turnover in neuronal growth cones. Nat Cell Biol. 2006;8: 215–226.
828 doi:10.1038/ncb1367

829 60. Murray A, Naeem A, Barnes SH, Drescher U, Guthrie S. Slit and Netrin-1 guide
830 cranial motor axon pathfinding via Rho-kinase, myosin light chain kinase and
831 myosin II. Neural Dev. 2010;5: 16. doi:10.1186/1749-8104-5-16

832 61. Brown JA, Wysolmerski RB, Bridgman PC. Dorsal root ganglion neurons react to
833 semaphorin 3A application through a biphasic response that requires multiple
834 myosin II isoforms. Molecular Biology of the Cell. 2009;20: 1167–1179.
835 doi:10.1091/mbc.E08-01-0065

836 62. Brown JA, Bridgman PC. Disruption of the cytoskeleton during Semaphorin 3A
837 induced growth cone collapse correlates with differences in actin organization and
838 associated binding proteins. Devel Neurobio. 2009;69: 633–646.
839 doi:10.1002/dneu.20732

840 63. Gallo G. RhoA-kinase coordinates F-actin organization and myosin II activity
841 during semaphorin-3A-induced axon retraction. J Cell Sci. 2006;119: 3413–3423.
842 doi:10.1242/jcs.03084

843 64. Fenix AM, Taneja N, Buttler CA, Lewis J, Van Engelenburg SB, Ohi R, et al.
844 Expansion and concatenation of non-muscle myosin IIA filaments drive cellular
845 contractile system formation during interphase and mitosis. Molecular Biology of
846 the Cell. 2016;27: 1465–1478. doi:10.1091/mbc.E15-10-0725

847 65. Albeg A, Smith CJ, Chatzigeorgiou M, Feitelson DG, Hall DH, Schafer WR, et al.
848 C. elegans multi-dendritic sensory neurons: morphology and function. Mol Cell
849 Neurosci. 2011;46: 308–317. doi:10.1016/j.mcn.2010.10.001

850 66. Shutova MS, Spessott WA, Giraudo CG, Svitkina T. Endogenous species of
851 mammalian nonmuscle myosin IIA and IIB include activated monomers and
852 heteropolymers. Curr Biol. 2014;24: 1958–1968. doi:10.1016/j.cub.2014.07.070

853 67. Shutova M, Yang C, Vasiliev JM, Svitkina T. Functions of nonmuscle myosin II in
854 assembly of the cellular contractile system. Parsons M, editor. PLoS ONE. Public
855 Library of Science; 2012;7: e40814. doi:10.1371/journal.pone.0040814

856 68. Nithianandam V, Chien C-T. Actin blobs prefigure dendrite branching sites. The
857 Journal of Cell Biology. 2018;217: 3731–3746. doi:10.1083/jcb.201711136

69. Luo L, Wen Q, Ren J, Hendricks M, Gershow M, Qin Y, et al. Dynamic encoding of perception, memory, and movement in a C. elegans chemotaxis circuit. Neuron. 2014;82: 1115–1128. doi:10.1016/j.neuron.2014.05.010

877 **FIGURE LEGENDS**

878 **Figure 1: UNC-6/Netrin signaling mediates sister dendrite self-avoidance.**

879 (A-B) Representative images and tracings of PVD sensory neurons in wild-type (A) and *unc-6* (B)
880 L4-stage larvae. PVD morphology was visualized with PVD::GFP or PVD::mCherry markers.
881 PVD cell body marked with an asterisk. (A) 1°, 2°, 3° and 4° dendritic branches and single axon
882 (blue arrowhead) are denoted. (B) Arrowheads point to overlaps between adjacent 3° dendrites
883 that failed to self-avoid in *unc-6* mutants. Scale bars are 5 μm. C) Summary of self-avoidance in
884 3° PVD dendrites denoting growth, contact and retraction. (D) Model of self-avoidance
885 mechanism involving reciprocal contact-dependent repulsion mediated by UNC-6/Netrin and its
886 receptors, UNC-40/DCC and UNC-5[9].

887

888 **Figure 2: Constitutively active UNC-5 drives hyper-retraction of 3° PVD dendrites.**

889 (A-D) Representative images and tracings of 3° dendrites anterior to PVD cell body in (A) wild
890 type (red) and (B) PVD::MYR::UNC-5 (blue) (Late L3-early L4 animals) (C) Gaussian fit to
891 distribution of lengths of PVD::mCherry-labeled 3° dendrites showing shorter average length for
892 MYR::UNC-5 (n = 156, 7 animals) *versus* wild type (n = 159, 8 animals), $p = 0.03$, Kolmogorov-
893 Smirnov statistical test. (D) Schematics of intact, wild-type UNC-5 receptor vs membrane-
894 associated, constitutively-activated myristylated-UNC-4 (MYR::MYR-5). (E-F) Dynamicity of 3°
895 dendrites in wild-type vs MYR::UNC-5-expressing PVD neurons labeled with PVD::GFP. (E)
896 Schematic (top) depicts displacement of the tip of a 3° dendrite relative to a fiduciary mark (vertical
897 dashed red line). Scale bar is 10 μm. Representative plots of displacement for wild-type (red) and
898 MYR::UNC-5 (blue) 3° dendrites over time. (F) The dynamic saltatory growth and retraction of
899 3° dendrites in the wild type vs the relative quiescence of MYR::UNC-5-expressing PVD neurons

900 is correlated with elevated standard deviation of tip movement from a fiduciary point in wild-type
901 vs MYR::UNC-5 expressing PVD neurons (p = 0.04 from Student's t-test. n = 4). (G) Self-
902 avoidance defects (percentage of overlapping 3° branches) are rare (< 5%) in wild type and
903 MYR::UNC-5. The *unc-6* self-avoidance defect is rescued by PVD expression of MYR::UNC-5.
904 Error bars denote mean and M. ***p<0.0001. n ≥ 15. from ANOVA with Tukey's posthoc test.
905 Scored in a PVD::mCherry background.
906
907 **Figure 3. Mutations in genes that promote actin polymerization disrupt PVD dendrite self-**
908 **avoidance.**
909 (A) Representative images (top) and schematics (bottom) of the actin cytoskeleton (Green) labeled
910 with PVD::ACT-1::GFP (A) and microtubules (Magenta) marked with *pdes-2*::TBA-1::mCherry.
911 PVD cell bodies (asterisks) and axons (arrowheads) are noted. (B) Representative images of
912 PVD::GFP for wild type, *unc-34*, *mig-10*, *unc-73*, *wsp-1* and *arx-5RNAi*. Asterisks denote PVD
913 cell bodies and arrowheads point to overlaps between adjacent PVD 3° dendrites. (C-E) Self-
914 avoidance defects are plotted in a PVD::GFP background (mean and SEM) as the percentage of
915 overlapping 3° dendrites for each genotype. ***p<0.001, *p<0.05, ANOVA with Tukey's posthoc
916 test, n ≥ 15 animals for all backgrounds. (C) Self-avoidance defects in *unc-73*, *mig-10* and *unc-*
917 *34/Ena/VASP* exhibit significant self-avoidance defects. *unc-34/Ena/VASP* mutants are rescued by
918 PVD expression of UNC-34 (PVD::mCherry::UNC-34). Myristyolated UNC-5
919 (PVD::MYR::UNC-5) fails to rescue the self-avoidance defects of an *unc-34* mutant. (D) PVD
920 self-avoidance defects for *arx-5RNAi*, *unc-6*, *wsp-1* and *unc-6; wsp-1* mutants and compared to
921 wild-type and E.V. *(Empty Vector) RNAi controls. ***p<0.001, NS = Not Significant, ANOVA
922 with Tukey's posthoc test, n ≥ 15 animals. Scale bar is 10 μm.

923

924 **Figure 4. Localization and trafficking of PVD::UNC-34::mCherry puncta in PVD.**

925 (A-B) Leica iSIM images of PVD neurons (late L3 larvae) labeled with PVD::LifeAct::GFP
926 (green) and PVD::mCherry::UNC-34 (Magenta). Merge shown at top right. Insets depict punctate
927 mCherry::UNC-34 in 1°, 2° and 3° PVD dendrites. (B) Note punctate mCherry::UNC-34 near
928 tips (white arrowheads) of 3° dendrites Scale bars are 5 μm. (C-D) Kymographs of
929 PVD::mCherry::UNC-34 in PVD 3° dendrite captured in the Leica iSIM microscope. Moving
930 (green arrowheads) vs stationary (red arrowheads) mCherry::UNC-34 puncta are denoted. The
931 distal end of the 3° dendrite is indicated by an asterisk and a red dashed arrow line points toward
932 the PVD cell soma. Scale bar is 10 μm.

933

934 **Figure 5. The actin cytoskeleton is highly dynamic in PVD dendrites.**

935 (A) Representative images of PVD::LifeAct::GFP and PVD::mCherry labeled 2° dendrite
936 undergoing outgrowth through time (late L3 larvae). (B) Fluorescent intensity was measured from
937 regions of PVD dendrites undergoing outgrowth vs no-outgrowth (see Materials and Methods).
938 ***$p<0.001$, N = 118 measurements from 6 dendrites. (C) Representative image showing enriched
939 LifeACT::GFP signal in distal, growing PVD dendrites labeled with PVD::mCherry. (D) Rapid
940 changes in the normalized fluorescence intensity of PVD::LifeAct::GFP versus the cytoplasmic
941 marker, PVD::mCherry, were quantified as the standard deviation of the normalized fluorescent
942 intensity measured at the tips of growing dendrites in a wild-type background. See Movie S3 and
943 Materials and Methods) N=22. (E) Normalized fluorescence intensity measurements of
944 PVD::LifeAct::GFP (green) vs cytoplasmic PVD::mCherry (red) at the tip of a growing late L3
945 stage PVD 3°dendrite from a representative time lapse movie

946

947 **Figure 6**: (A-D) Fluorescent intensity traces in wild-type PVD dendrites during 3° dendrite contact
948 based self-avoidance. Fluorescent intensity measurements of PVD::LifeAct::GFP and
949 PVD::mCherry were acquired from a 1μm region at the tip of the growing and contacting left and
950 right 3° dendrites (Late L3-L4 animals). Measurements were normalized against the maximun
951 intensity during a ~10 minute interval that includes at least one contact event. The cytoplasmic
952 mCherry signal was used to measure the gap between the left and right 3° dendrites undergoing
953 contact and plotted against time. The period of contact (vertical shading) corresponds to a
954 minimum value for the gap (0-0.14μm) between contacting left and right 3° dendrites. (E)
955 Representation of 3° dendrites with color schemes to indicate left and right 3° dendrites and regions
956 quantified. (F) Measurements from contact and non-contact (control) regions of 3° dendrites
957 undergoing self-avoidance did not detect a significant increase in LifeAct::GFP at contact between
958 the tips of adjacent 3° dendrites. Normalized LifeAct::GFP fluorescence intensity values from
959 these regions (see Materials and Methods) were plotted vs time, N = 8, NS = Not Significant, 2-
960 way ANOVA with Bonferroni correction.

961

962 **Figure 7. NMY-1/non-muscle myosin II mediates dendrite self-avoidance**.
963 (A) Representative images (left) and tracings (right) of wild-type and *nmy-1(sb113)* labeled with
964 PVD::GFP. PVD cell soma (asterisks) and overlapping 3° dendrites (arrowheads) are noted. The
965 PDE neuron is marked with an asterisk and is adjacent to the PVD cell-body. (B) NMY-1 fused to
966 GFP via a linker peptide (PVD::GFP::NMY-1) (top) expressed in PVD with PVD::mCherry
967 (bottom) rescues self-avoidance defects (C) of *nmy-1(sb113)*. Scale bars are 5µm. (D)
968 Quantification of self-avoidance defects in wild type and *nmy-1*. Self-avoidance defects for *nmy-*

969 *1* mutants and *nmy-1* cell-specific RNAi (csRNAi) increase the percentage of overlapping 3°
970 branches. PVD expression of GFP-labeled NMY-1 (PVD::GFP::NMY-1) rescues the *nmy-*
971 *1(sb113)* self-avoidance defect. Scatter plots with mean and SEM, ***p<0.01, One way ANOVA
972 with Tukey's posthoc test. N = 15-20 animals per genotype. All defects were quantified in a
973 PVD::GFP background. Scale bar is 5 μm.
974
975 **Figure 8. Phosphomimetic activation of myosin regulatory light chain, MLC-4, shortens 3°**
976 **PVD dendrites and rescues the *unc-6* dendritic self-avoidance defect.**
977 (A) Phosphorylation of Regulatory Light Chain (RLC) induces a conformational change that
978 activates the myosin protein complex composed of myosin heavy chain (MHC), essential light
979 chain (ELC) and RLC. (B) Threonine and serine phosphorylation sites (red) in conserved regions
980 of *C. elegans*, *Drosophila* and human myosin RLCs. (C) Phosphomimetic construct,
981 PVD::GFP::MLC-4-DD, fused to GFP with a linker peptide for expression with PVD promoter.
982 (D-E) Representative images (top) and schematics (bottom) of PVD morphology anterior to cell
983 body (asterisk) denoting 3° dendrites for (D) wild type (red) and (E) MLC-4DD (blue) (L3 stage
984 larvae). Wild-type image also used in Figure 2A. Scale bars are 10 μm. 3° dendrite length (F) is
985 shorter and gaps between 3° dendrites (G) is wider for MLC-4DD versus wild type. Gaussian fit
986 was plotted with bin center values (μm) on the X-axis and the number of values that fall under
987 each bin center on the Y axis, ***p<0.001, Kolmogorov-Smirnov statistical test for cumulative
988 distributions of PVD 3° dendrite lengths and length of gaps in MLC-4DD (n = 141, 6 animals)
989 versus wild type (n = 156, 8 animals). (J) PVD expression of MLC-4DD rescues the *unc-6* mutant
990 self-avoidance defect, ***p<0.0001, One way ANOVA with Tukey's posthoc test. Mean and
991 SEM are shown. n ≥9 animals per genotype. Quantified with PVD::mCherry. Scale bar is 10 μm.

992

993 **Figure 9. Opposing pathways regulate dendrite outgrowth and retraction.**

994 Representative images and schematics of PVD in (A) *kpc-1/kpc-1*, (B) *kpc-1/+; unc-6/+* and (C)

995 *kpc-1 +/+ dma-1; unc-6/+*. PVD soma (asterisks) and overlapping 3° dendrites (arrowheads) are

996 noted. (D) Quantification of self-avoidance defects for each genotype. Note that all mutant alleles

997 are recessive but that *kpc-1/+; unc-6/+* double heterozygotes show a strong self-avoidance defect

998 that is suppressed in *kpc-1 +/+ dma-1; unc-6/+* triples. ***$p<0.0001$, one way ANOVA with

999 Tukey's posthoc test. Mean and SEM are indicated. N >7 animals per genotype. PVD is labeled

1000 with *ser2prom3*::GFP for all images. Scale bar is 10 μm. Mutant alleles were: *kpc-1(xr58), unc-*

1001 *6(ev400)* and *dma-1(wy686)*. (E) Model of opposing pathways that promote actin polymerization

1002 to define dendrite length. KPC-1 antagonizes surface expression of DMA-1 that interacts with an

1003 epidermal receptor composed of SAX-7/CAM, MNR-1 and LECT-2 and functions with HPO-30

1004 to promote actin polymerization and dendrite outgrowth. UNC-6/Netrin interacts with UNC-5 to

1005 activate UNC-34/Ena/VASP which functions with WSP-1/WASP and the Arp2/3 complex to drive

1006 F-actin assembly for NMY-1/myosin-dependent dendrite retraction in the self-avoidance response.

1007

1008

1009

1010

1011

1012

1013 **SUPPORTING INFORMATION.**

1014 **Imaging and quantification of self-avoiding 3° dendrites:** L3 animals of strain
1015 CLP928 *twnEx382[Pser2.3::LifeAct::EGFP, Pser2.3::mCherry, Pgcy-8::gfp]* [34] were
1016 immobilized for time-lapse imaging with 1μl of agarose beads (Polybead carboxylate
1017 microspheres, Polysciences, Catalog # 15913-10, 0.05 μm) and mounted on a 10% agarose pad.
1018 Z-stacks of PVD dendrites (0.5 um depth, 5 slices) were imaged at 35 second intervals with a 40X
1019 objective on a Nikon spinning disk confocal microscope. Contact between the 3° dendrites was
1020 established as a function of Max Feret (maximum distance between 2 points). Max Feret (in pixels)
1021 was measured in the mCherry channel (cystosolic marker) with NIS elements and contact defined
1022 as by the time-point at which the Max-Feret approaches zero. LifeAct::GFP and mCherry signals
1023 were measured for a ROI of 2 μm at the tips of the left and right dendrites in a single Z plane. Left
1024 and right fluorescence intensities were summed for comparison to a control ROI (2 μm). The
1025 change in fluorescence intensity (ΔF) for each contact and control region was calculated as the
1026 difference between the signal at contact (F_t) and the fluorescence value at two time points prior to
1027 contact (F_{t-2}) normalized to F_{t-2} or $\Delta F = (F_t - F_{t-2})/F_{t-2}$ [34]. These values were computed for
1028 contact and control ROIs for LifeAct::GFP and mCherry. Statistical tests used for comparison
1029 between the datasets (LifeAct::GFP contact vs control, mCherry contact vs control, LifeAct::GFP
1030 contact vs. mCherry contact) were 2-way ANOVA with Bonferroni correction and multiple t-tests
1031 with a False Discovery Rate of 1%. Both these tests yielded similar results.

1032

1033

1034 **Supplemental Figure 1. Mutations in *unc-34/Ena/VASP* and *unc-73/Trio* disrupt PVD**
1035 **dendrite morphology.**

1036 (A) Quantification of 1° dendrite outgrowth and (B) number of 2° dendrites in wild-type, *unc-34*,
1037 *unc-73*, *wsp-1* and PVD::mCherry::UNC-34;*unc-34*. Defective 1° dendrites show altered
1038 alignment and/or extension defects. Mutations in *unc-34* and *unc-73* but not *wsp-1* exhibit defects
1039 in 1° dendrite outgrowth and fewer 2° dendrites. Note that cell-autonomous expression of UNC-
1040 34::mCherry does not rescue 1° and 2° dendritic defects but does restore self-avoidance (Figure
1041 3C). (C) Representative images of PVD morphological defects in an *unc-34* mutant. Note
1042 premature termination of 1° dendrites (red arrowheads). Scale bars are 10 μm. Mutant alleles are
1043 *unc-34(gm104), unc-73(rh40), wsp-1 (gm324).*
1044
1045 **Supplemental figure 2.** (A) Schematic (left) of adjacent 3° dendrites and representative time
1046 lapse series (35 sec intervals) of PVD::mCherry and PVD::LifeAct::GFP in 3° dendrites showing
1047 self-avoidance response. Point of contact is indicated by an asterisk and period of contact denoted
1048 with dashed blue outline. Scale bar is 10 μm. (B) Schematic depicting ROIs for fluorescence
1049 intensity measurements at the tips of adjacent (left vs right) 3° dendrites that undergo contact and
1050 at an adjacent non-contact (control) region. (C-E) Graphical representation of the change in
1051 fluorescence intensity at each time point vs that of the t = -2 time interval before contact at t = 0;
1052 measurements were normalized to th[34] (See Materials and Methods). Normalized fluorescence
1053 intensity values were plotted against time (min) for (C) LifeAct::GFP contact vs control, (D)
1054 LifeAct::GFP contact vs mCherry contact, (E) mCherry contact vs mCherry control. The values at
1055 each time-point were compared by 2-way Anova with Bonferonni correction, NS (Not Significant)
1056 N=14.
1057

1058 **Movie S1: Time-lapse video representing the dynamic movement of 3° dendrites in a wild-**
1059 **type background.** Images of PVD::GFP were recorded (late L3-early L4) at 15 sec intervals with
1060 a 100X objective in a Nikon spinning disk microscope (see Materials and Methods). The entire
1061 length of the video is 240 seconds. The movie was edited using NIS elements software with Bayes
1062 advanced denoising. Green arrowheads denote the tips of 3° dendrites. Scale bar is 25 μm.
1063
1064 **Movie S2: Time-lapse video of 3° PVD dendrites in a MYR::UNC-5 background.** Images of
1065 PVD::GFP in the MYR::UNC-5 strain were recorded (late L3-early L4) at 15 sec intervals with a
1066 100X objective in a Nikon spinning disk microscope (see Materials and Methods). The entire
1067 length of the video is 12 minutes. Boxes denote tips of 3° dendrites showing limited outgrowth**.**
1068 The movie was edited using NIS elements software with Bayes advanced denoising. Scale bar is
1069 10μm.
1070
1071 **Movie S3: Time-lapse video showing the dynamicity of LifeAct::GFP during in 3° PVD**
1072 **dendrites**. Images of PVD::mCherry (left) and PVD::LifeAct::GFP (right) and were collected at
1073 1.3 min intervals with a 100 X objective in a Nikon spinning disk microscope (see Materials and
1074 Methods). The entire length of the video is 60 minutes. The movie was edited using NIS elements
1075 with automatic deconvolution. Scale bar is 5 μm. Spherical objects are autofluorescent granules.
1076
1077 **Movie S4: Time-lapse video demonstrating the rapid accumulation of LifeAct::GFP after**
1078 **contact between 3° sister dendrites**. Images of PVD::mCherry (left) and PVD::LifeAct::GFP
1079 (right) and were collected at 1.3 min intervals with a 100 X objective? in a Nikon spinning disk
1080 microscope (see Materials and Methods). The entire length of the video is 60 minutes. The movie

1081 was edited using NIS elements software with automatic deconvolution. Arrows track the moving

1082 3º dendrite undergoing contact and retraction. Scale bar is 5 μm.

1083

1084 Movie S5: **Movie S5: Time-lapse video demonstrating the rapid accumulation of**

1085 **LifeAct::GFP after contact between 3° sister dendrites**. Images of PVD::LifeAct::GFP were

1086 captured at 15 second intervals using a 100X objective in a Nikon TIRF microscope for a total of

1087 25 minutes at the L3-L4 stage (see Materials and Methods). The movie was edited using NIS

1088 elements with Bayes advanced denoising. The bottom panel depicts a fluorescence intensity profile

1089 through time (bottom) for the ROI (green). Scale bar is 5 μm.

1090

1091

1092

1093

1094

Figure 1: PVD 3° dendrites undergo self-avoidance in an UNC-6/Netrin dependent manner

A. wild-type

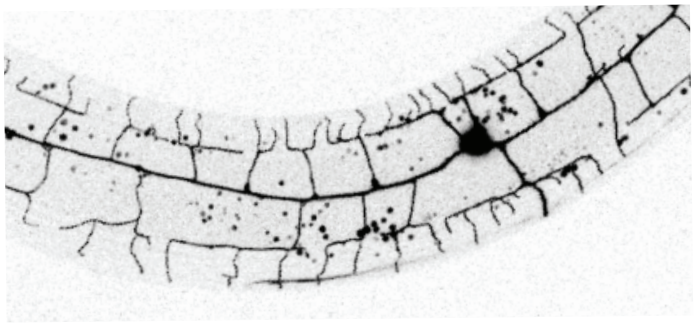

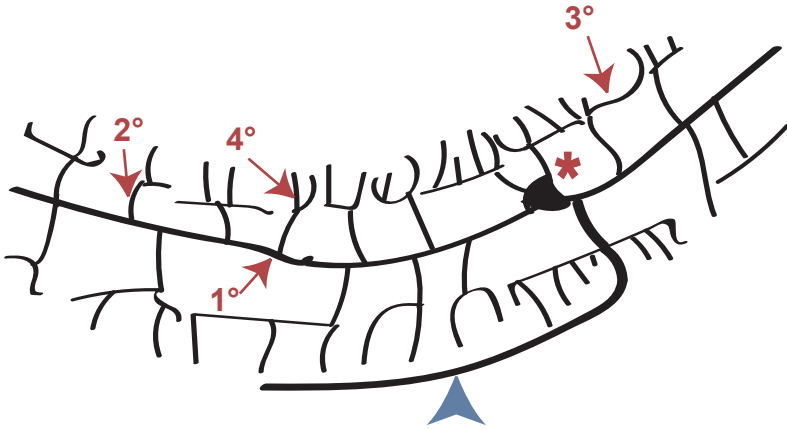

B. *unc-6*

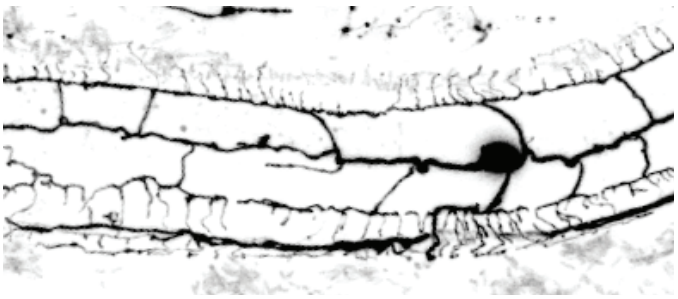

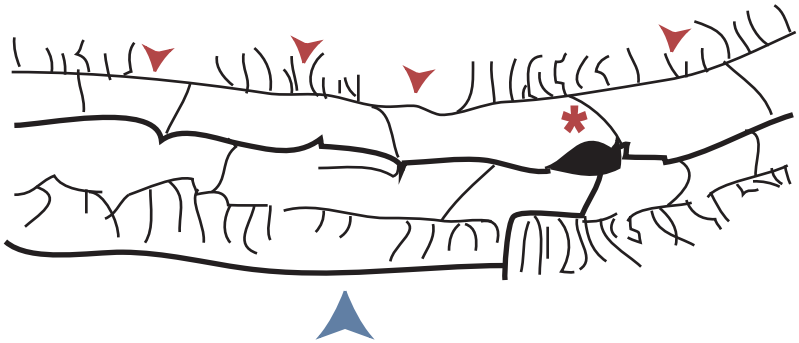

C.

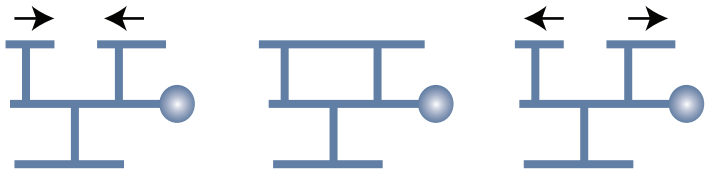

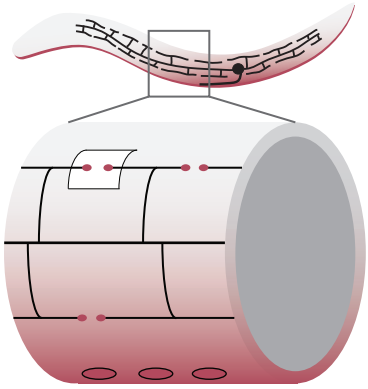

UNC-6 expressing cells

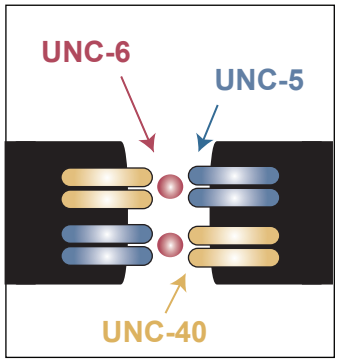

Figure 2: Constitutively active UNC-5 drives hyper-retraction of 3º PVD dendrites.

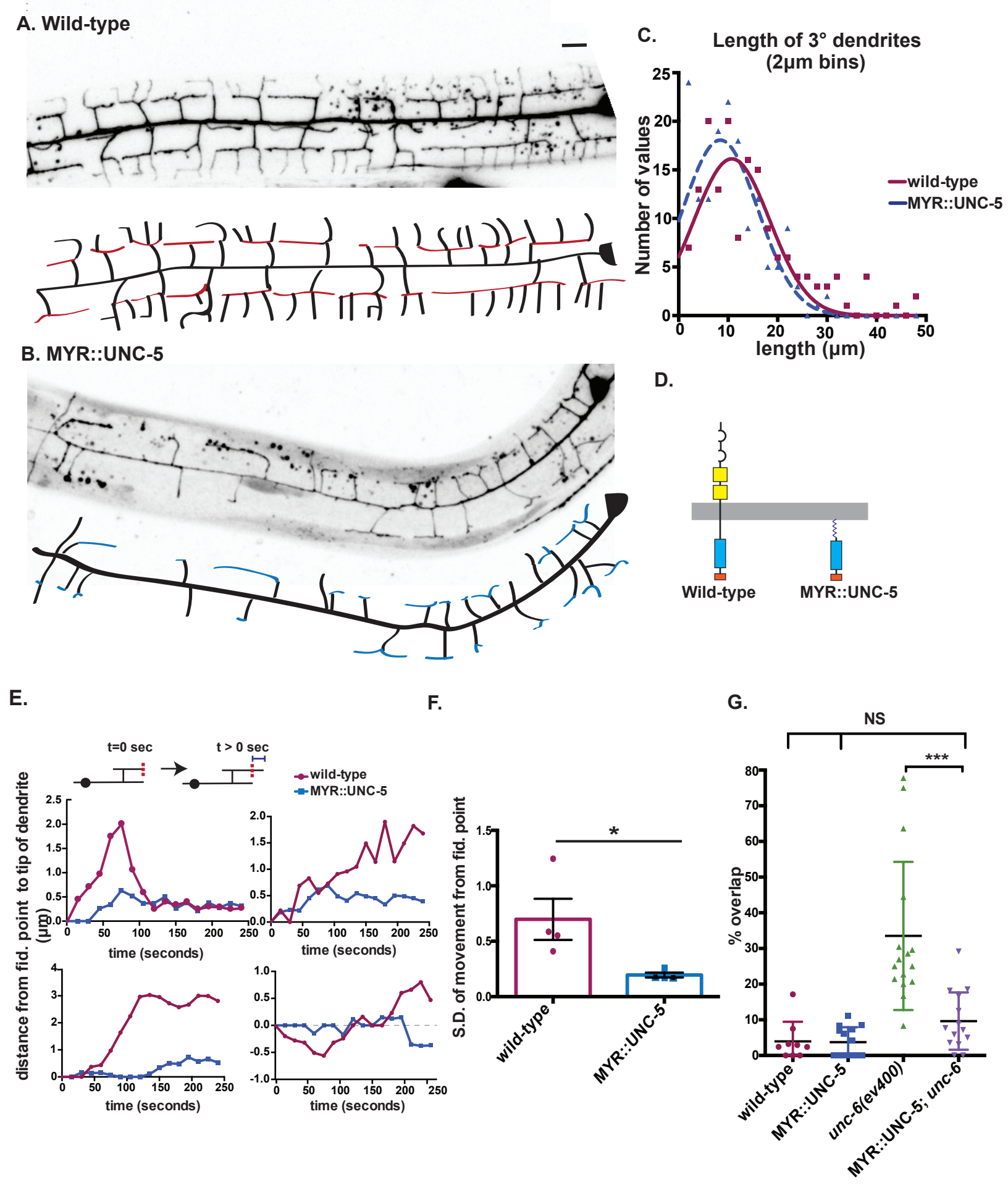

Figure 3: Mutations in genes that promote actin polymerization disrupt PVD dendrite self-avoidance.

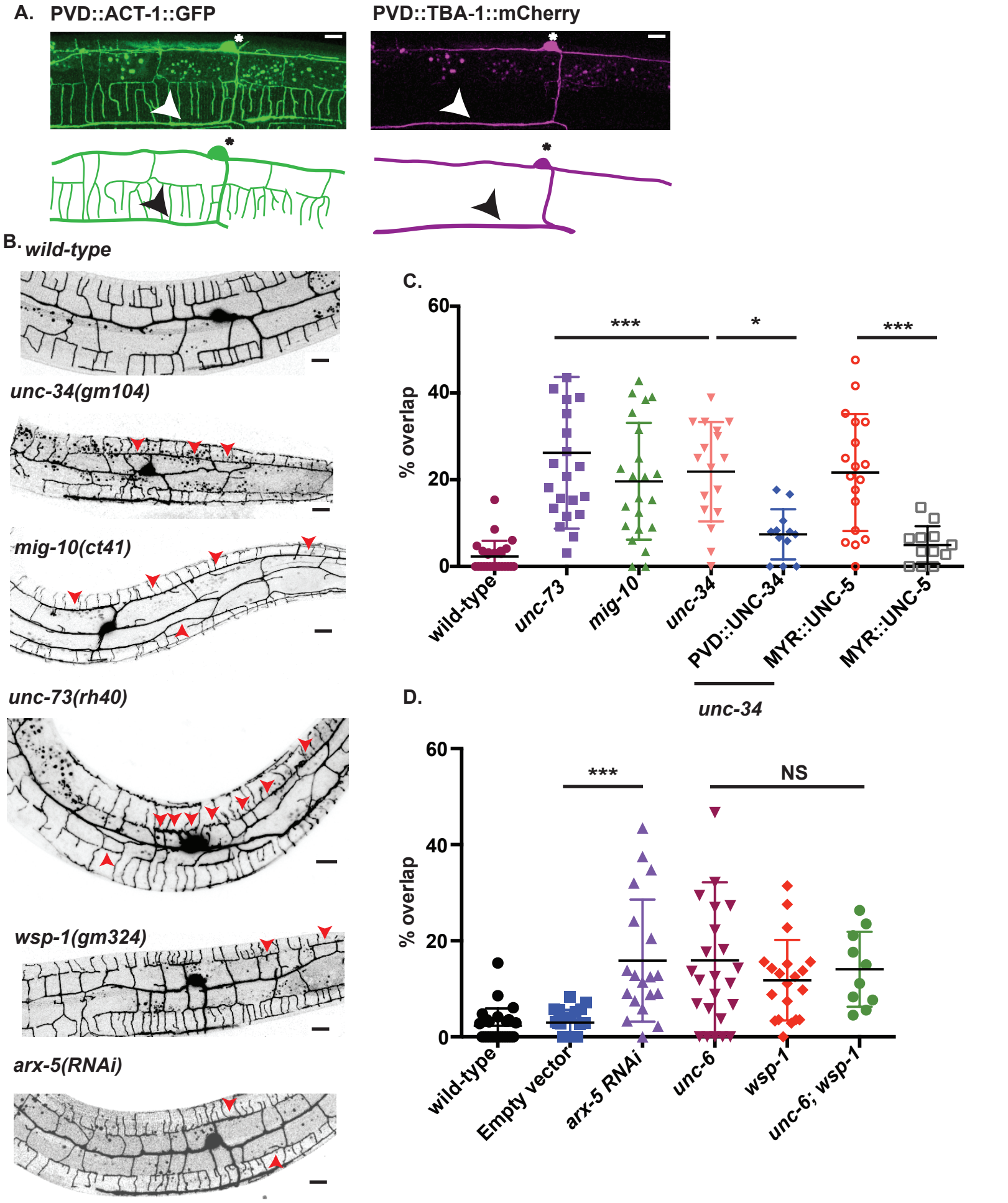

Figure 4: Localization and trafficking of PVD::UNC-34::mCherry puncta in PVD.

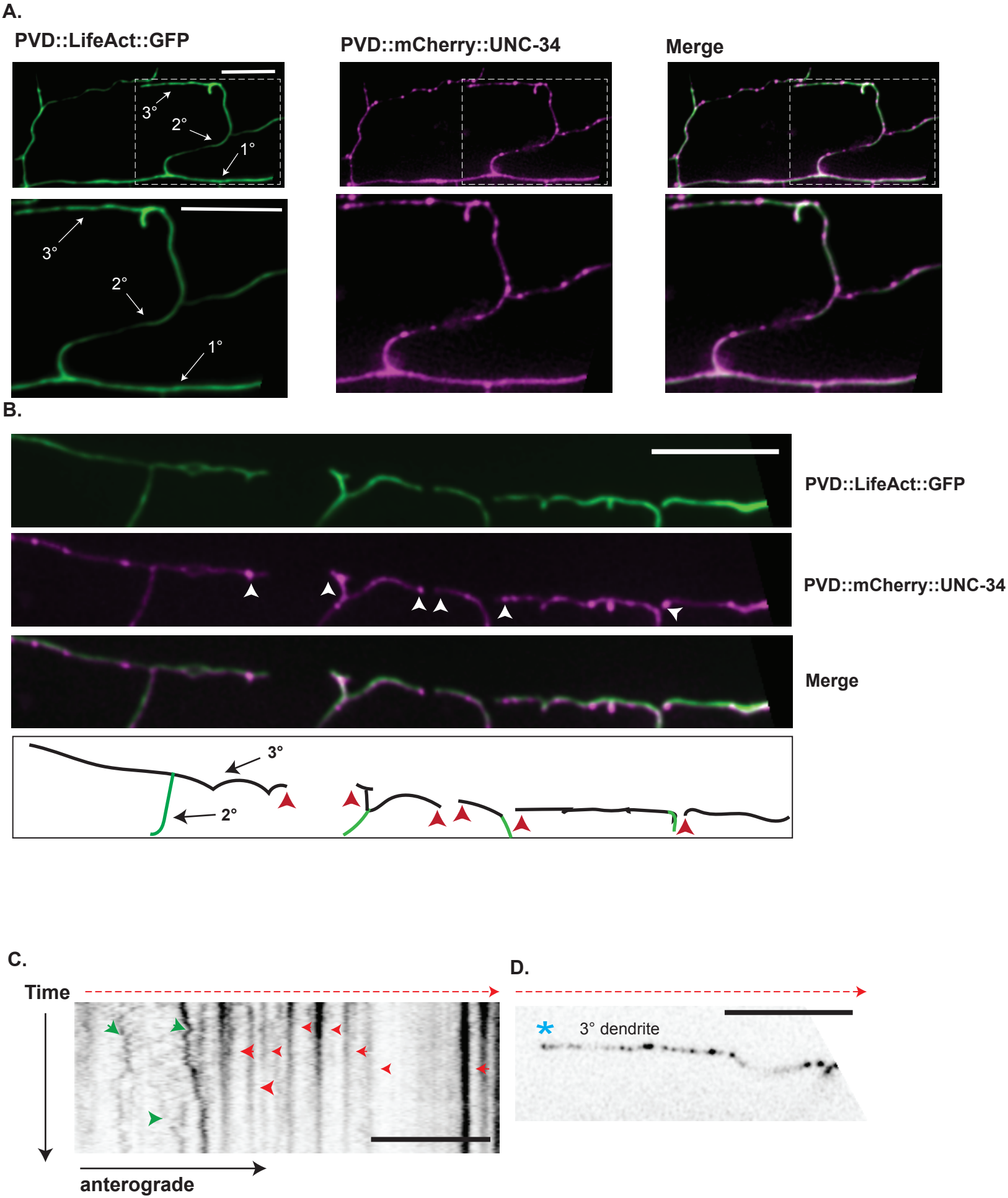

Figure 5: The actin cytoskeleton is highly dynamic in PVD dendrites

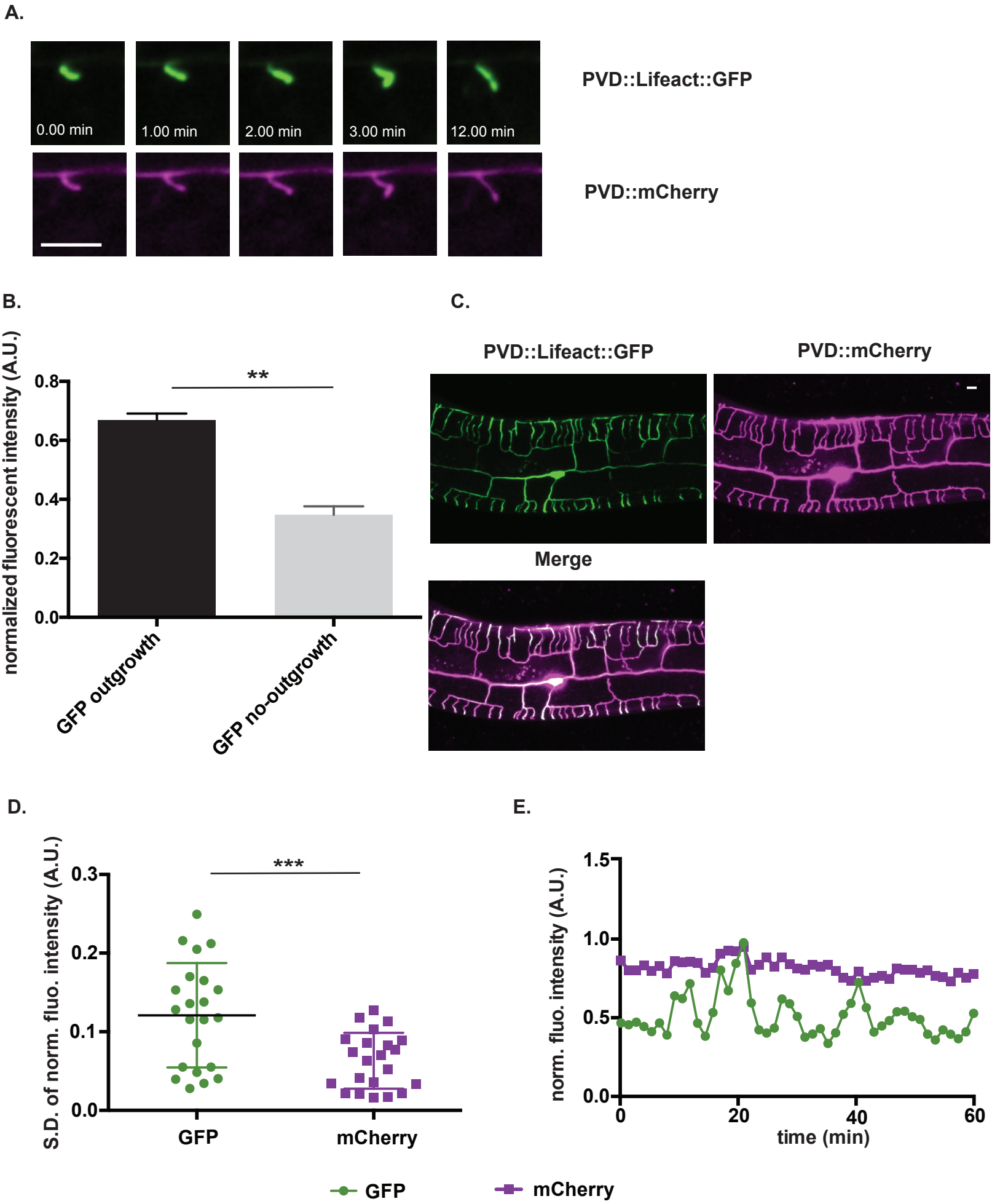

Figure 6: Dynamic changes in actin polymerization during contact based retraction

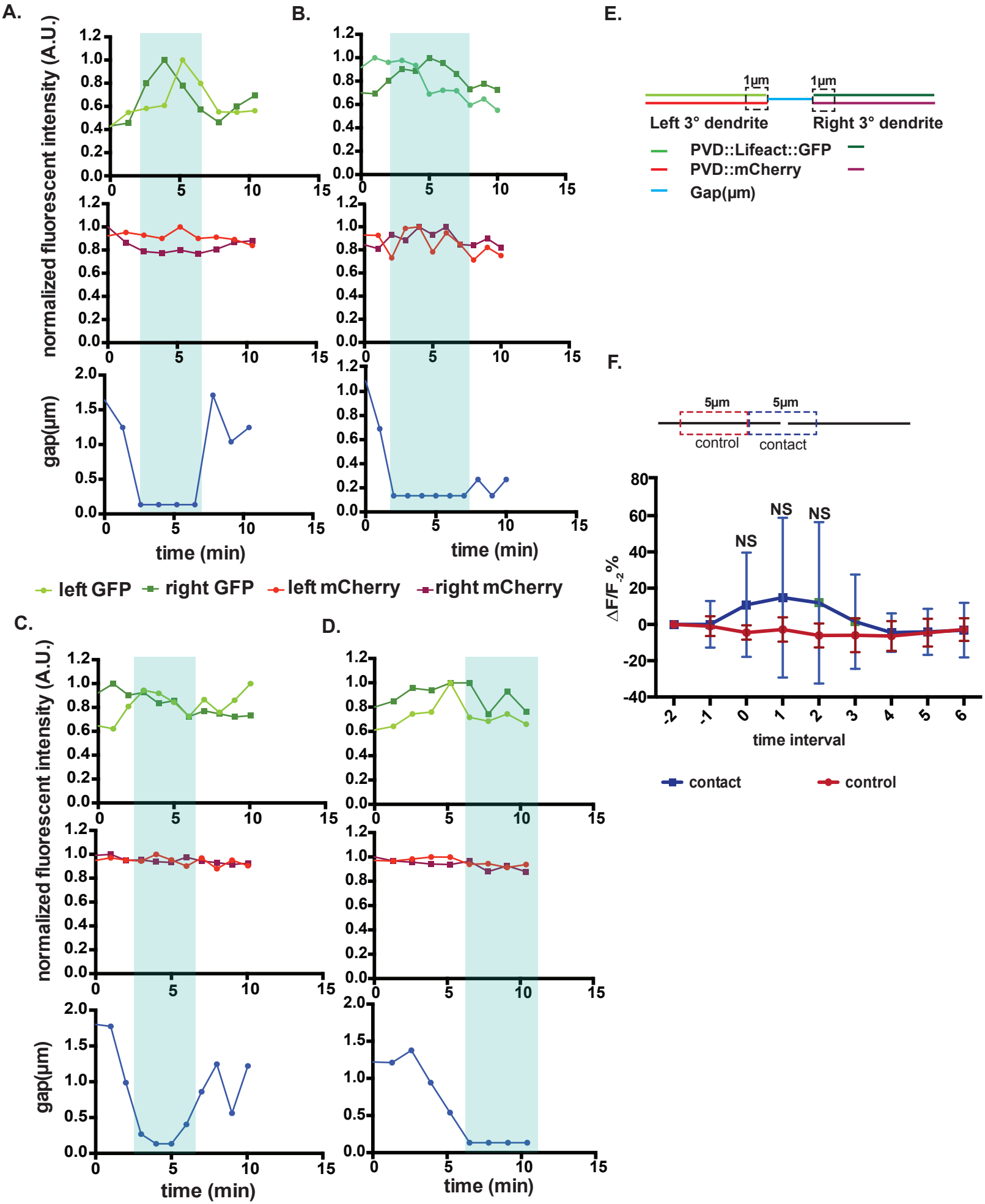

Figure 7: NMY-1/non-muscle myosin II mediates dendrite self-avoidance.

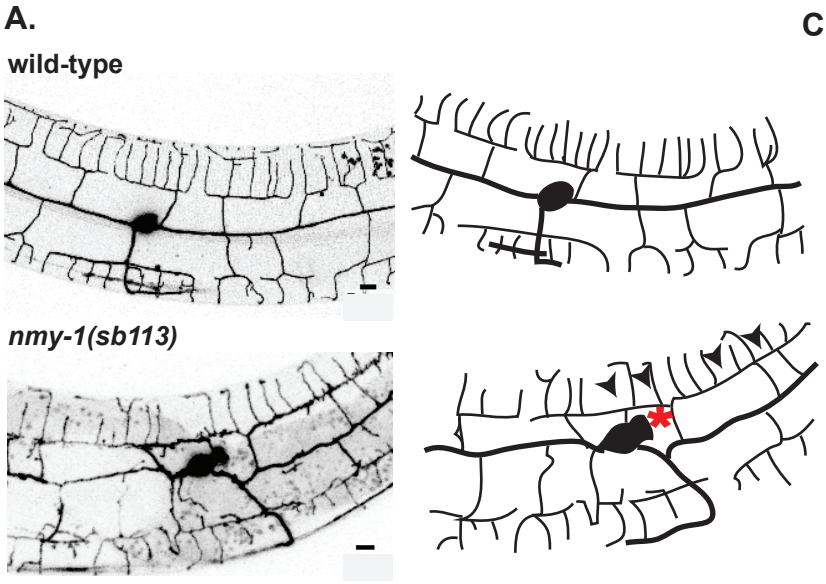

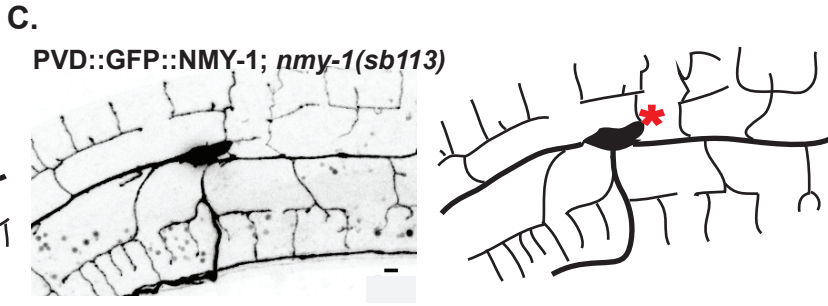

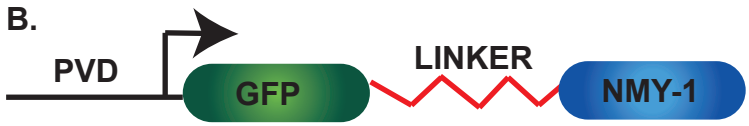

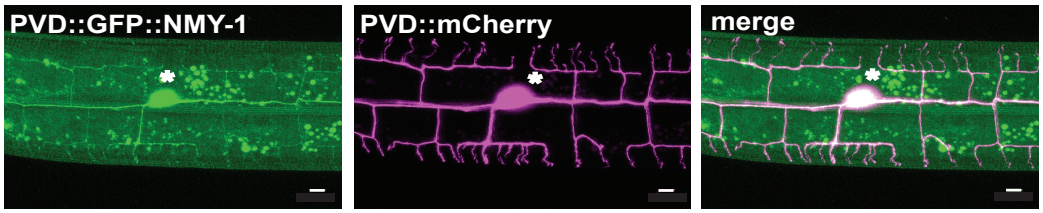

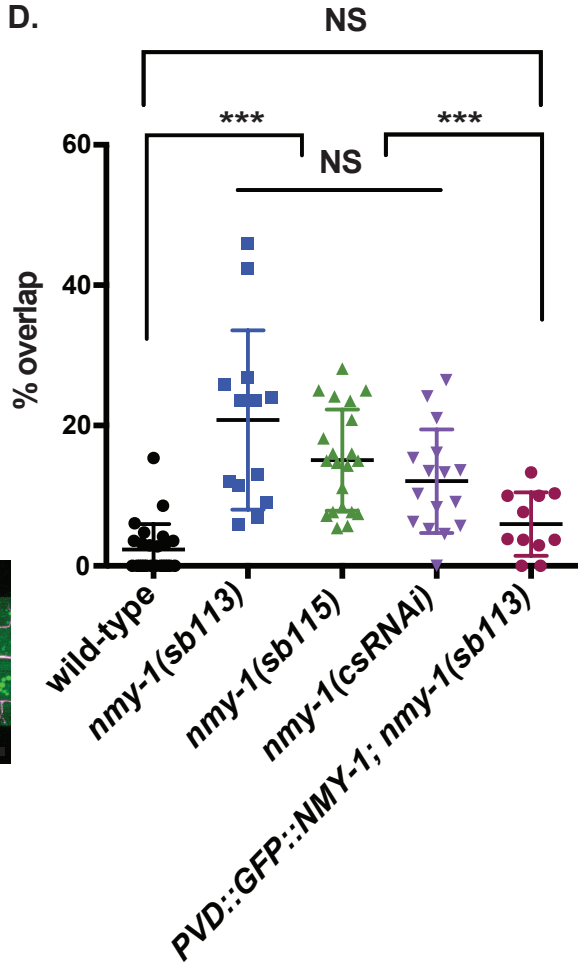

Figure 8: Phosphomimetic activation of myosin regulatory light chain, MLC-4, shortens 3º PVD dendrites and rescues the *unc-6* dendritic self-avoidance defect.

A.

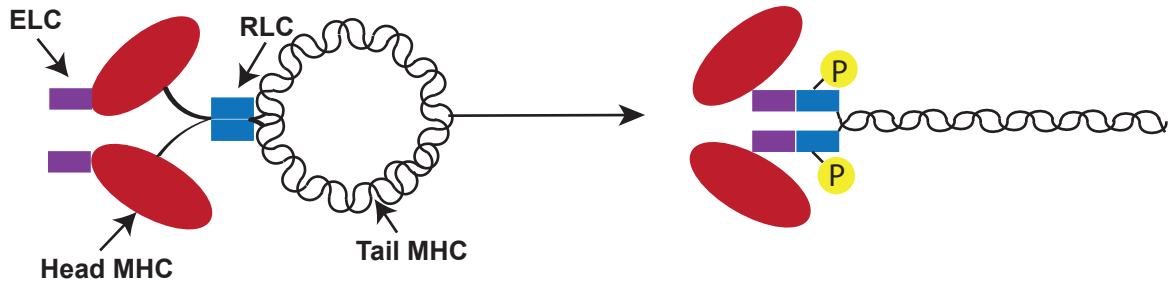

B.

C. elegans	MLC-4	QRATSNVFAMFDQ
D. melanogaster	MRLC-C	QRATSNVFAMFDQ
H. sapiens	MRLC2	QRATSNVFAMFDQ

C.

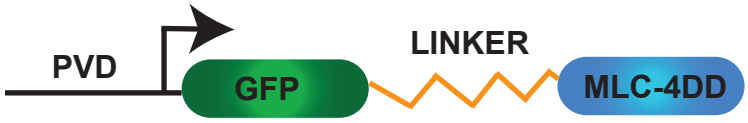

D.

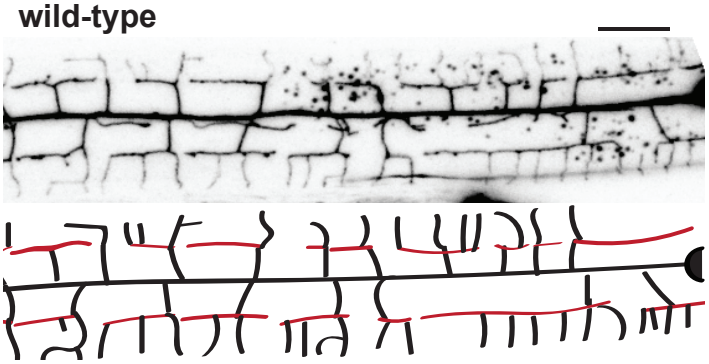

E.

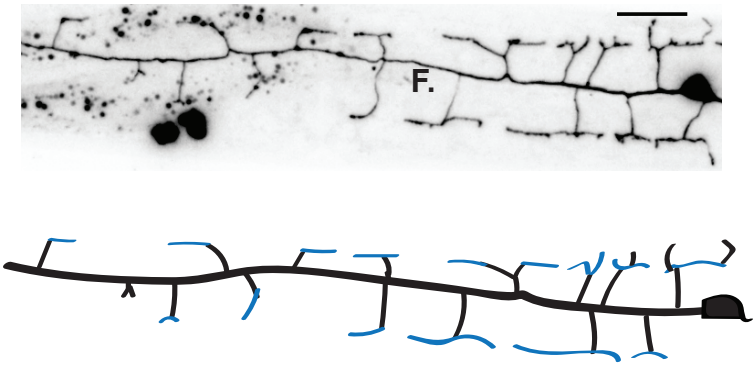

F.

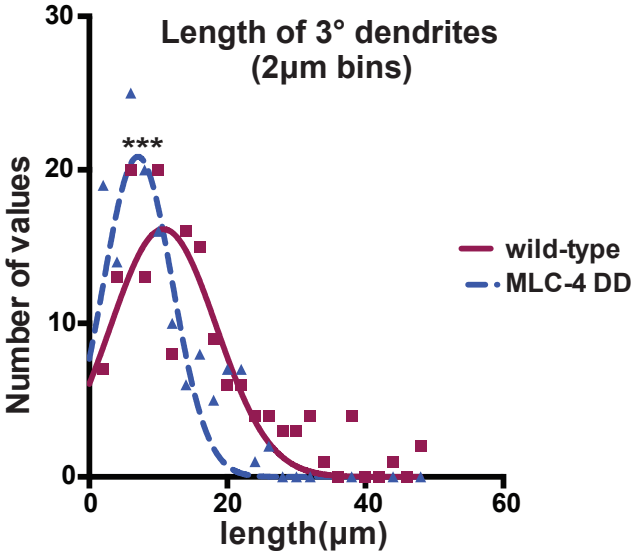

G.

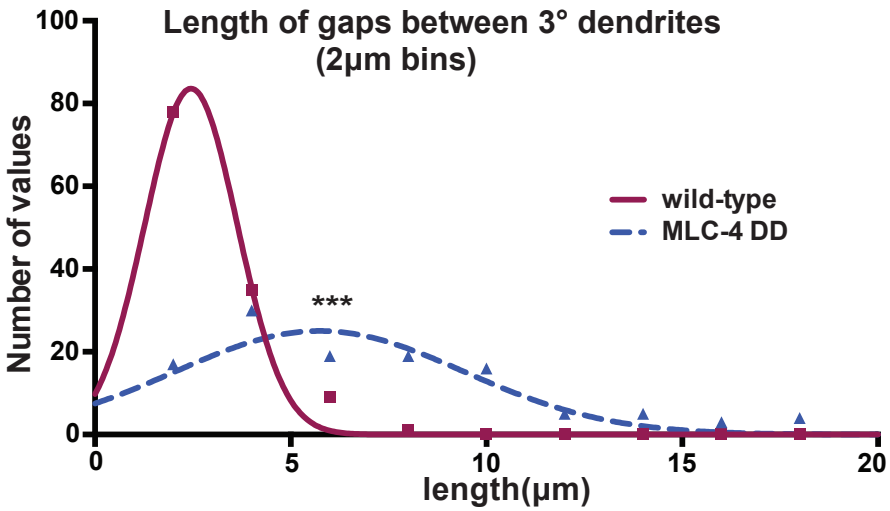

H.

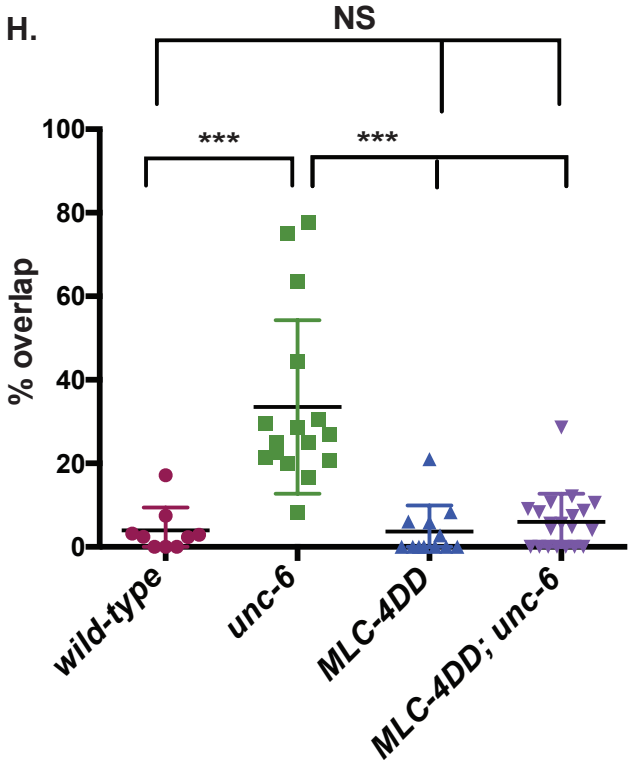
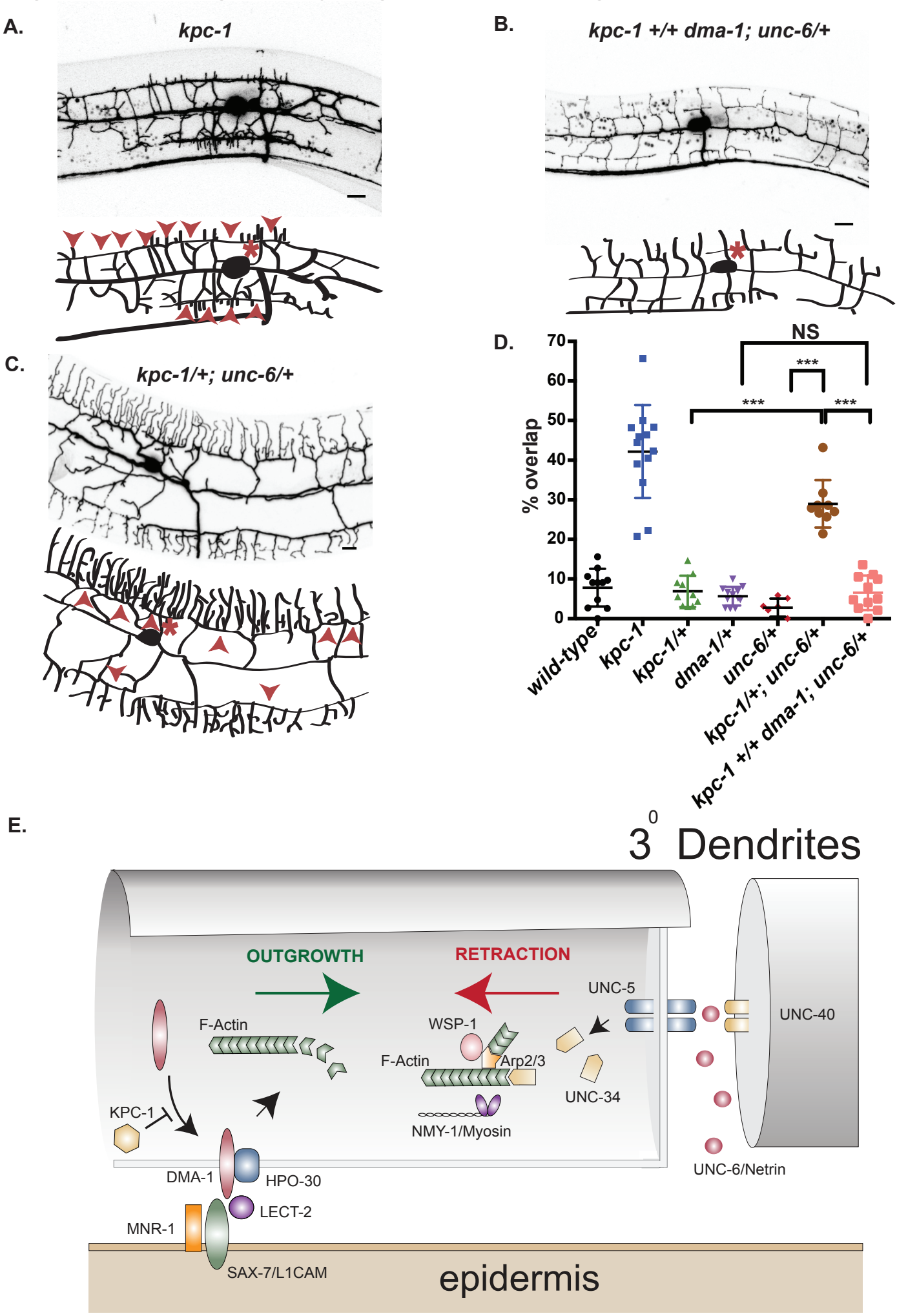
Figure 9: Opposing pathways regulate dendrite outgrowth and retraction.